UiO : Department of Physics
University of Oslo

Nuclear Structure and Dynamics in the Quasi-Continuum of ^{240}Pu

Fabio Zeiser

Master's Thesis, Spring 2016

Abstract

Nuclear level densities and γ-ray strength functions are essential quantities in various fields of basic and applied research involving nuclear matter. From microscopic calculations and structure research to nuclear reactor models and astrophysical applications a good knowledge of these parameters determines fundamental properties of the systems. This study analyses the level density and strength function of ^{240}Pu below the particle separation threshold with the Oslo Method. The results are used to examine the effect on the fast neutron capture cross-section of ^{239}Pu.

At the Oslo Cyclotron Laboratory a ^{239}Pu target was bombarded with a 12 MeV deuteron beam to study (d,pγ) reactions in the quasi-continuum of ^{240}Pu. The particle-γ coincidences were used to obtain the primary γ-rays and extract level density and γ-ray strength function of ^{240}Pu using the Oslo Method.

This new experimental data reveals an increase in the γ-ray strength function on the tail of the Giant Electric Dipole Resonance, which is interpreted as a low-energy M1 scissor mode. The $B(M1)$ strength of this resonance between about 2-4 MeV has been estimated and is compared to previous findings in the actinide region.

Furthermore, these results were used to calculate the (n,γ) cross-sections for ^{239}Pu with the TALYS reaction code. This provides predictions for neutron energy regions where previously no experimental data was available and may have a significant impact on calculations for next generation reactors.

Acknowledgements

Although writing up a thesis might be the effort of one person, just to get so far as to be able to start writing is only possible due to the invaluable help of many other people. I am grateful for everyone who has been there to support me, both scientifically and personally.

I would like to express my sincere gratitude to my supervisors Sunniva Siem and Magne Guttormsen. Your doors have always been open to me. Thank you, Sunniva, not only for the valuable input to my thesis, but also all the time you devoted to discussions on my (hopefully bright) future. I am indepted for the liberty to participate in many more projects then only this work. I hope I will have as much patience and insight as Magne when explaining the same details of the method time and again. I also thank Gerald Kirchner for his supervision.

Many thanks to Gry Tveten and Ann-Cecilie Larsen for sharing a manifold of interesting thoughts with me and for your generous scientific support. Although you do not have an official role in the supervision of this thesis, I could not have achieved the same results without you. I am most grateful for Thibault Laplace for numerous discussion and the similarities you have pointed out in our data. Thanks to Therese Renstrøm for your willingness join my efforts to study equation prefactors with pen and paper.

The atmosphere in this group is fantastic and all of you have made it a pleasure to be here! A special thanks for everyone's efforts at day and night to make the experiment possible. Sparing no efforts, many others have helped with a night or two or three at the cyclotron: Lee Bernstein, Darren Bleuel, Josh Brown, Matthieu Lebois, Mathis Wiedeking and Jon Wilson. Thanks to the excellent engineers at the Cyclotron for their hands-on support to deliver perfect experimental conditions.

I would like to thank my dear friends Morten and Pär for helping me to overcome many obstacles with a bright smile: Tenting outside in a light snow storm was just about the best thing to do when you need distracting from a potentially boring three months with a cast around your wrist! Thanks Angjerd for introducing us and keeping my spirits high (above the clouds). I am grateful for all the year of studies and comradeship that connect me with Johannes and I hope one day we will live door-by-door again.

I owe a big thanks to my family that has been most loving and encouraging and for accepting silently, that I once more live far away from home.

Finally, I wish to acknowledge the generous financial support of the German National Academic Foundation. My time in Norway would not have been possible without it.

Thank You!

Fabio Zeiser

February 2016

Contents

1 Chapter 1. Introduction

The story so far:
In the beginning the Universe was created.
This has made a lot of people very angry and
been widely regarded as a bad move.

Douglas Adams
The Hitchhiker's Guide to the Galaxy

More than 100 years after Rutherford's discovery of the atomic nucleus in 1911, basic questions on structure and properties of the nucleus still remain open. This work aims to investigate the level density and γ-ray strength function in the actinide region, in particular for ^{240}Pu. In addition, the relevance of the results for other fields like the study of advanced nuclear reactors and astrophysics is shown. To set the stage for the current analysis, a brief overview of the historical and the scientific context is given.

In March 1911 Ernest Rutherford gave the first public presentation on the experimental work on the nature of the atom that had been conducted over the previous two years by Hans Geiger, Ernest Marsden and himself [1]. From the angular distribution of α-particles scattered off a thin gold foil, he deduced that the prevailing theory of the atom as a plum pudding, composed of electrons and surrounded by a big positive charge distribution, had to be replaced. Instead, he put forward the theory of the atom as known today, with the protons forming the nucleus and electrons orbiting around it in the distance of a few ångstrøms. Soon after this, speculations arose about the additional existence of neutral particles in the nucleus, however it was only in 1932 that James Chadwick was able show the presence of the neutron [2]. By the end of the second world war, many of the most famous experiments in nuclear physics had been conducted, amongst them the activation of elements though neutron bombardment by Enrico Fermi [3] and the neutron-induced fissioning of ^{238}U by Lise Meitner, Otto Hahn, Fritz Strassmann and Otto Robert Frisch [4]. With an astonishing foresight for the applications of this new knowledge, these experiments would within only a few years lead to the first nuclear reactors and nuclear weapons.

With the simultaneous development of quantum mechanics, a theoretical framework was established in which the energy levels of a nucleus and transitions between them could be described. For higher excitation energies and nuclear masses, the spacing between the levels reduces greatly, thus forming a (quasi-)continuum of states. Then, the concept of discrete levels

looses its relevance and one usually considers level densities and average transition strengths. However, *ab initio* calculations to obtain these are today and in the foreseeable future only feasible for few particle systems. Several methods have been introduced to enlarge the range of nuclei accessible to theoretical predictions, for example the Monte Carlo Shell Model [5] or the Hartree-Fock-Bogoliubov plus combinatorial method [6]. Still, these are constrained by the computational power and limited knowledge of the prevailing nucleon-nucleon interactions.

In this context it is essential to obtain experimental data on level densities and γ-ray strength functions. The latter is a reformulation of the transition probability which takes out the direct energy dependence that emerges from a quantum mechanical treatment of the transition operators; for a detailed derivation of this dependence see Ref. [7, p.595]. Several well known experimental techniques exist to extract nuclear level densities like the particle evaporation [8] and two-step cascade [9] method. However, both require prior knowledge, in the first case of optical model parameters, and in the second case a model of the γ-ray strength function. A new method is coming up that utilizes high-energy light-ion reactions, see e.g. Ref. [10] using $(\mathrm{p}, \mathrm{p}')$ and $(\mathrm{e}, \mathrm{e}')$ with energies of 200 MeV and 56 MeV respectively, to infer information on discrete levels. This is essential in detailed tests of level density models. However, a major constrain to the latter technique is that it requires level spacings in the order of, or larger, than the experimental resolution.

The present work uses the Oslo method [11, 12], which has the unique feature that it allows the simultaneous extraction of level density and γ-ray strength function in the quasi-continuum without prior assumption of a model for these function. The method uses data below the neutron separation threshold from particle-γ coincidences of inelastic scattering, like $(\mathrm{p}, \mathrm{p}'\gamma)$, and transfer reactions, like $(^3\mathrm{He}, \alpha\gamma)$. In this thesis the $(\mathrm{d}, \mathrm{p}\gamma)$ reaction on ^{239}Pu will be analyzed.

In the last years there has been an increasing effort to systematically study properties of nuclei in the actinide region. Previous publications using the Oslo method include analyses for $^{231-233}$Th, $^{232-233}$Pa, $^{237-239}$U [13–15], ^{238}Np [16] and ^{243}Pu [17]. The resulting level densities follow a constant temperature formula and thereby challenge the back-shifted Fermi-gas model. The latter includes pairing effects to the groundbreaking work of Bethe [18] in 1936, which was the first theoretical attempt to describe nuclear level densities for heavy nuclei. As the back-shifted Fermi-gas model has been widely used and is still a common reference, see for example the data library RIPL3 [19], it is interesting to test the model's validity for level densities of more actinide nuclei.

In addition to the level densities, the γ-ray strength function will be analyzed in this thesis. Early (γ, n) experiments revealed a strong resonance at excitation energies around 10-14 MeV known as the Giant Electric Dipole Resonance (GEDR) [20]. In a macroscopic picture, this is explained by protons oscillating against neutrons. As common for resonating systems, a Lorentzian shaped response was assumed, which describes well the data around the peak of the GEDR. However the above named publications using the Oslo Method [13–17] as well more recent (γ, γ') and $(\mathrm{e}, \mathrm{e}')$ experiments [21–23] reveal an excess of strength between about 1 and 4 MeV on the tail of the GEDR.

This additional resonance is interpreted as the scissors mode. Name-giving is here the classical explanation of protons oscillating like scissor blades against neutrons, although a recent review by Heyde et al. [24] clearly shows the benefit and necessity of a microscopic explanation. Such an additional resonance may have a significantly impact on the branching ratio between γ decay and other decay modes like fission and particle emission. The second aim of this study is to find out the presence and potential strength of a scissors resonance in ^{240}Pu.

The resulting level density and γ-ray strength function of ^{240}Pu, including a potential scissors resonance, are essential inputs to calculations of the (n,γ) cross-section of ^{239}Pu within a statistical framework [25]. Although there is accurate knowledge of the cross-section for thermal and low-energy neutrons, one has little reliable experimental information on fast neutrons. Without this constrain, predictions from major nuclear data libraries like ENDFB/VII.1 [26] and JENDL-4.0 [27] reveal discrepancies of up to about half an order of magnitude for incident neutron energies above 0.5 MeV. Thus the reference article to ENDFB/VII.1 states that "[t]hese reactions are so important that should new assessments, based on new measured data, lead to significant changes in these evaluated cross sections, there will be significant implications for nuclear applications, for example in our criticality calculations." [26]

This applies in particular for the assessment of fast neutron reactors, where the ratio of fast neutron induced fissions over neutron captures and scattering is a key parameter. Recent studies on the data needs for such systems by the OECD Nuclear Energy Agency (NEA) usually demand target accuracies for the cross-sections well below 10 % [28, 29]. It is thus of direct relevance to these analyses to obtain more accurate calculations of the (n,γ) cross-sections for actinides.

In addition, studying a nucleus for which at least partially experimental data exists can be regarded as a contribution to a validity test for cross-section calculations based on data extracted with the Oslo method. With this technique, it is also possible to access nuclei which pose a major challenge to direct experiments determining the cross-section due to e.g. short half-lives. However, those nuclei may have a significant impact on the estimation of the abundance of heavy elements in the universe. In fact, rapid neutron capture is the only process that can lead to the formation of actinides and a large number of cross-sections enter the calculations of their synthesis [30]. In return, this means that from their abundances given e.g. from meteoroid samples, it is possible to infer the age of the universe.

Common to all these applications is that the goodness of the model predictions is to a large extent limited by the quality of the input data. This work explores the level density and γ-ray strength function of ^{240}Pu and improves knowledge of the $^{239}\mathrm{Pu}(\mathrm{n},\gamma)$ cross-section for fast neutrons. In addition it contributes to a an understanding of the systematics of various properties in the actinide region.

The thesis is organized in the following way: After this short introduction, the next chapter will explore the experimental set-up and the technique to obtain particle-γ reactions from the $^{239}\mathrm{Pu}(\mathrm{d},\mathrm{p})$ reaction. Chapter 3 introduces the Oslo method and the level density and γ-ray strength function for ^{240}Pu are extracted. Furthermore, this data is used to calculate the $^{239}\mathrm{Pu}(\mathrm{n},\gamma)$ cross-section. In Chapter 4 we discuss the context and significance of the results. Finally, in Chapter 5 the main findings are summarized and put into perspective with upcoming research .

Chapter 2.
2 Experimental setup and data extraction

"Doc, you don't just walk into a store and-and buy plutonium! Did you rip that off?"
"Of course. From a group of Libyan nationalists. They wanted me to build them a bomb, so I took their plutonium and, in turn, gave them a shoddy bomb casing full of used pinball machine parts."

Back to the Future

2.1. The Oslo Cyclotron Laboratory

The heart and core of the Oslo Cyclotron Laboratory (OCL) is the Scanditronix MC-35 cyclotron, that produces a pulsed ion beam. For this experiment a deuteron beam was chosen in order to study the (d, p) reaction as a substitute with controlled energy deposit for (n, γ) reactions. The beam was tuned to 12 MeV with an intensity of about 1 nA.

2.1.1. Experimental setup

The experimental setup at OCL is shown in Figure 2.1. The facility is divided into an inner hall where the cyclotron itself and auxiliary magnets are located, and an outer hall containing both detectors, labeled CACTUS and SiRi and the target. After the particles have been accelerated, the beam is focused and bended by several dipole D_i and quadrupole Q_i magnets. The switching magnets can be used to deliver beam to other experiments such as radio-isotope production. Finally the beam passes though a set of collimators and magnets to be focused on the target inside the detector array.

The data extraction method utilized in this thesis is based on a simultaneous measurement of charged particles and γ-rays created in the ^{239}Pu(d,p)^{240}Pu reaction. The $0.4\,\mathrm{mg/cm^2}$ thick ^{239}Pu target was purified by an anion-exchange resin column procedure [32] prior to electroplating it on a $1.9\,\mathrm{mg/cm^2}$ beryllium backing.

A ring of silicon detectors (SiRi) [33] shown in Figure 2.2 is used to measure the energy of the charged particles. Each of the eight detector strips consists of eight thin ($\sim 130\,\mu$m) silicon

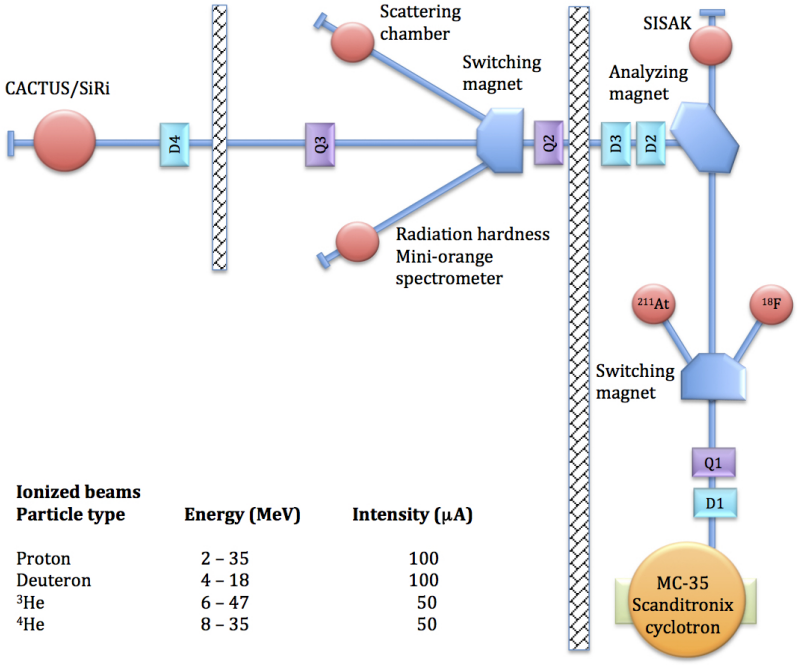

Ionized beams

Particle type	Energy (MeV)	Intensity (μA)
Proton	2 – 35	100
Deuteron	4 – 18	100
^{3}He	6 – 47	50
^{4}He	8 – 35	50

Figure 2.1.: Schematic of the OCL with target stations. The inset shows beams that have been experimentally realized with the possible energy regions and intensities. Reproduced from [31].

pads in which the particles loose a fraction of their energy, thus being called ΔE detectors. The latter are mounted in front of a silicon pad (labeled E detector) that is so thick ($\sim 1550\,\mu$m) that it stops the particle and thereby absorbs all the remaining energy. This results in a total of 64 $\Delta E - E$ detectors covering azimuthal angles from $126° - 140°$. In front of all detectors there is a $10.5\,\mu$m aluminum foil to shield δ-electrons. Figure 2.2a illustrates one of the detector strips, giving the angular coverage of each single ΔE detector. The placement with respect to target and beam is shown in Figure 2.3a. The beam energy was chosen as high as possible, however such that the outgoing particles are still fully stopped in the E detector, thus enabling to measure the full energy of the particle.

Surrounding SiRi, the CACTUS array [34] detects the emitted γ-radiation and consists of 26 lead collimated NaI(Ti) crystals. Each crystal is 5″x5″ (12.7x12.7 cm) large and mounted on a spherical frame as can be seen in Figure 2.3b. Taking into account the reduced diameter $r = 3.5\,$cm due to the lead collimators, the fraction of the total solid angle covered by the detectors is $\Omega = \frac{N\pi r^2}{4\pi R^2} = 16.4\%$. Here N denotes the number of detectors and $R = 22\,$cm is the distance between target and detector. For the 1332-keV γ-transition in ^{60}Co the efficiency was measured to be 14.1(2)% and the relative energy resolution is $\sim 6\%$.

Recently the Nuclear Instrument for Fission Fragments (NIFF) [35] has been included inside CACTUS in order to detect and veto fission events. The new low-pressure proportional counter, more specifically a Parallel Plate Avalanche Counter (PPAC), detects heavy ions. The name is derived from that fact that the heavy ions of importance at the OCL are fission fragments. The detector's intrinsic efficiency was measured with a ^{252}Cf source to be more than 90%

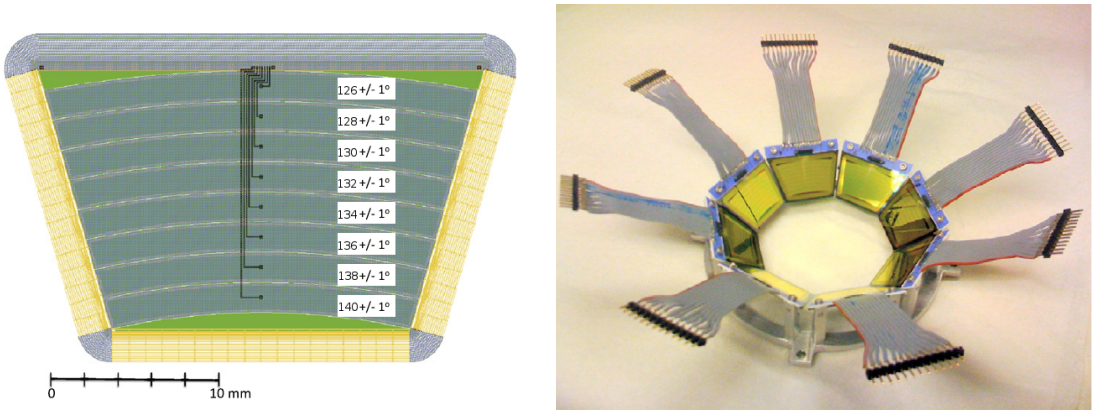

(a) (b)

Figure 2.2.: The SiRi particle detector, (a) shows the layout of one silicon chip with its eight ΔE detectors for the different reaction angles. The whole detector including cables to read out the signal is shown in (b). Adapted to backwards angles from [33].

for an incoming fragment. The design of the detector was limited by the available space and the presence of SiRi inside CACTUS. As the fission fragments have an opposing impulse, a geometric coverage of 60% of 2π leads to a total efficiency of 55(2)%. A recent study by Ducasse et al. [36] carefully re-analyzed the geometrical and total efficiency taking into account simulations of the angular anisotropy effects in the center-of-mass system for ^{238}U(d, p) with 18 MeV deuterons. The obtained total efficiency was (48.0 ± 3.5)%, which is adopted in this work.

More information on the detectors and the acquisition electronics can be found in [33, 34, 37] and references therein.

2.2. Energy calibration and particle identification

2.2.1. The particle detectors

Bombarding a heavy nucleus like ^{239}Pu with deuterons leads to a manifold of reactions. A crucial component in our data analysis is the selection of particle-γ coincidences from the same nuclear reaction. Thus we have to distinguish between the various ejectiles. For this purpose we can take advantage of the stopping powers of charged particles in the detector material, which depend i.a. on velocity, mass and charge of the particle. A more detailed description of the interaction of light ions with matter and the average energy loss is given by the Bethe-Bloch formula [38, 39]

$$\frac{\mathrm{d}E}{\mathrm{d}x} = 2\pi N_a r_e^2 m_e c^2 \rho \frac{Z}{A} \frac{z^2}{\beta} \left[\ln\left(\frac{2m_e\gamma^2 v^2 W_{\max}}{I^2} - 2\beta \right) \right], \tag{2.1}$$

where following variables have been used:

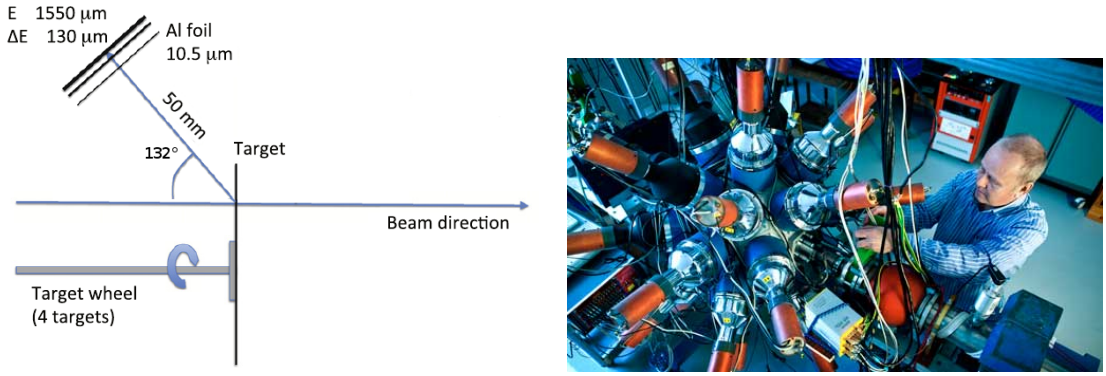

(a) (b)

Figure 2.3.: Detector setup. (a) displays the placement of SiRi of with respect to target and beam and (b) shows a picture of the complete setup of the CACTUS array. Picture reproduced from [31].

N_a	Avogado constant	z	charge of the ionizing particle
r_e	electron radius	v	speed of the particle
m_e	electron mass	β	v/c
c	speed of light	γ	Lorentz factor $1/\sqrt{(1-\beta^2)}$
ρ	density of absorber	$W_{\max}$	maximum energy transfer in a collision
A	mass number of absorber	I	mean excitation potential

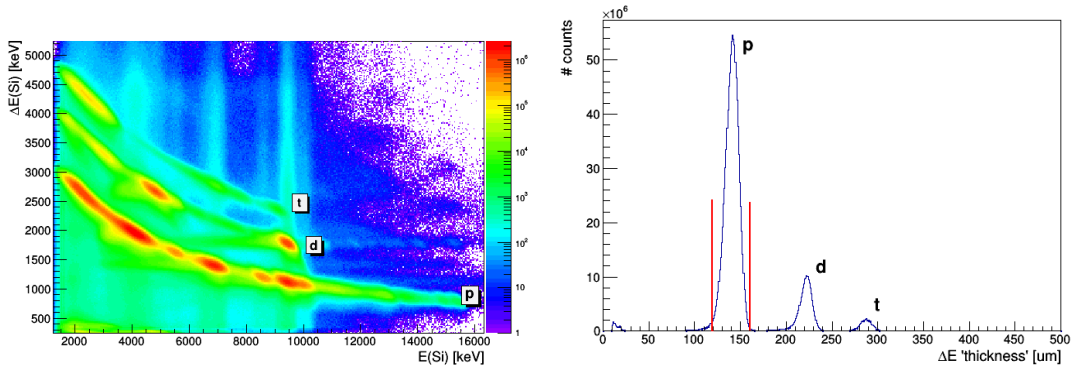

(a) (b)

Figure 2.4.: (a) Energy deposited in SiRi's front and back detectors, E and ΔE respectively. (b) Corresponding apparent thickness spectrum used to identify the ejectiles. The vertical lines indicate the gates set to extract only (d, p) reactions. The small labels denote the ejectiles.

If we plot the energy deposited in the ΔE against the energy deposited in the E detectors, this leads to a separate "banana" shape for each ejectile shown in Figure 2.4a.

Every individual particle detector has to be calibrated. A linear correlation is assumed between the true energy E and the channel number ch that is read out from the SiRi detector

$$E = a_o + a_1 \times ch, \tag{2.2}$$

where a_0 is commonly denoted as the energy shift and a_1 as the gain. These coefficients can be determined if there are two calibration points, i.e. points of known energy in each spectrum.

The expected energy calibration points can be obtained with the Bethe-Bloch equation (2.1). With a beam energy known from the cyclotron settings we calculate the energy loss in the target and detectors. It has to be taken into account that the distance the ejectile travels through the target depends on the scattering angle θ. Thus each of the eight detectors of a strip will give slightly different deposited energies. The impact of the angular dependent recoil energy is negligible, as the target nucleus ^{239}Pu is much heavier than the projectile. At last, for all inelastic reactions of type $\mathrm{a} + \mathrm{X} \rightarrow \mathrm{Y} + \mathrm{b}$ the reaction Q value must be added to the ejectile energy (due to differences in the binding energy and configuration of the nucleus)

$$Q = (m_\mathrm{a} + m_\mathrm{X} - m_\mathrm{Y} - m_\mathrm{b})c^2, \tag{2.3}$$

where we have used the masses m_i of the projectile a (i.e. deuterons), the target X (i.e. ^{239}Pu), the nucleus Y created by the reaction, and the ejectile b, respectively.

The actual calculation were performed with "SiRi Kinematics Calculator" by A. Bürger [40], combining the different steps with a user-friendly graphical interface. A makeshift solution shown in Figure 2.5 was necessary to adopt the real target configuration to a usable input by the program. Figure A.1b in the appendix is an example of a so called "banana plot" for the scattering angle $\theta = 140°$, calculated for known discrete excitation levels of the residual nucleus (i.e. ^{240}Pu in the (d, p) reaction) and interpolated between these. The maximum energy transfer to the ejectile occurs when it leaves the nucleus in its ground-state: This marks the (easiest) calibration points at rightmost end of the "bananas". Due to the good statistics the ground-state of ^{239}Pu from ^{239}Pu(d,d$'$)^{239}Pu was chosen as a calibration point besides ^{240}Pu ground-state from ^{239}Pu(d,p)^{240}Pu. The results are listed in Table 2.1.

The (d,d$'$) ground-state is clearly visible and it is also confirmed by magnetic spectrograms from Ref. [41] that it is strongly populated in this reaction. The (d, p) ground-state can be more difficult to establish; the rightmost end of the (d, p) banana is displayed in Figure A.2 (of the appendix). Comparisons with a magnetic spectrum from Friedman and Katori [42] reprinted in the appendix, Figure A.3, in fact show a roughly 600 keV broad region which contains little to no counts. This can only be reproduced by our data if the second peak to the right is assumed to be the (d, p) ground-state. The rightmost peak probably stems from contamination by another nucleus. Although contaminations should only form a small fraction of the target, differences in the (d,p) reaction probabilities could explain that both peaks have almost the same intensity.

Several peaks from nuclei other than ^{239}Pu need to be taken into account in the latter analysis. These include reactions with the ^{16}O contamination of the target and the ^{9}Be backing. Note that there is also another contamination peak at approximately 14.4 MeV visible in Figure A.2. It stems from a light nucleus, as for light masses the recoil leads to considerable angular dependent energy shifts. The deposited energy fits well with calculations for ^{27}Al, the target frame material.

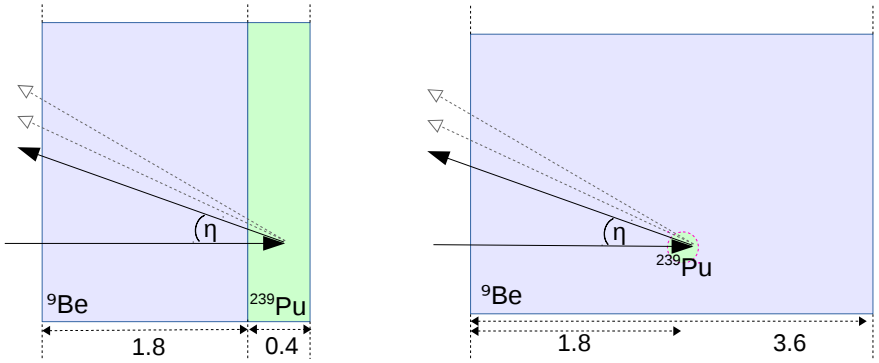

(a) (b)

Figure 2.5.: The ^{239}Pu target on its ^{9}Be backing, where the particle trajectories are indicated by arrows for different scattering angles $\theta = 2\pi - \eta$. The material thickness is given in mg/cm^2. (a) The actual scattering target used in the experiment. (b) Workaround to enable calculations with "SiRi Kinematics Calculator" where ^{9}Be is chosen as the "target" whilst keeping ^{239}Pu as scattering isotope.

2.2.2. Particle discrimination: The apparent thickness

As the goal of the analysis is to find level densities and strength-functions related to the (d,p) reaction, we have to select the corresponding events. Here we can again utilize the Bethe-Bloch formula Eq. (2.1), now in a reversed manner, with the calibrated particle spectra as input data. The apparent thickness of the ΔE detector for protons is retrieved and plotted in Figure 2.4b. Events of the (d,p) reaction will result in an apparent thickness near the real value of 130 μm. One observes a distribution around a central peak which is due to the statistic nature of the interaction of ions with matter: The Bethe-Bloch formula describes only the average energy loss. However, as the proton peak is well separated from the other ejectiles, it is without limitations possible to gate on its apparent thickness and therefore to extract only (d,p) reactions. The applied gate from 120 to 150 μm is highlighted in the plot.

Table 2.1.: Calibration points for the SiRi spectra for different reactions at 12 MeV beam energy. Values are given in keV. The detector rings are numbered according to each scattering angle θ.

Ring	Θ	E (d,p)	E (d,d′)	ΔE (d,p)	ΔE (d,d′)
0	140°	14915.8	9454.5	785.2	1781.1
1	138°	14920.8	9461.8	782.2	1774.1
2	136°	14924.7	9466.2	780.2	1769.5
3	134°	14927.3	9467.7	779.2	1767.3
4	132°	14928.8	9466.1	779.1	1767.5
5	130°	14929.1	9461.3	780.0	1770.1
6	128°	14928.0	9453.2	781.9	1775.1
7	126°	14925.5	9441.5	784.9	1782.6

2.2.3. The γ-ray detectors

Similarly to the particle detector, the NaI(Tl) detectors are calibrated assuming a linear correlation between true energy and the recorded channel number. The chosen reference points are the γ-rays from contaminants and backing of the target: the first excited state in ^{17}O at 870 keV and in ^{10}Be at 3367 keV respectivly. The energies were retrieved from the ENSDF database [43, 44]. The plausibility of this calibration was checked by identifying the remaining peaks; more information on this follows in Section 2.4.

2.3. True and random coincidences: The time spectrum

Coincidences between γ-rays and particles are recorded with a time-to-digital converter (TDC). Each charged particle detected in SiRi gives a start signal and a stop signal is created upon registration of a γ-ray by a NaI(Tl) detector. A typical TDC spectrum is shown in Figure 2.6a, where each timing bin is about 2.4 ns wide. The stop signal is delayed by about 200 bins which is longer than the cyclotron's beam pulse period. Thus we need to distinguish between true and random coincidences. An example for the latter would be a γ-ray detected in coincidence with a particle from a previous beam burst. The strong peak at about bin 200 contains true and random coincidences for one given beam burst. Figure 2.6a also shows a gate of equal width chosen long after the first beam burst which therefore only contains random coincidences. The true events are obtained by subtracting the events in the the random gate (bin 300 to 330) from those that fall into the peak gate (bin 190 to 220).

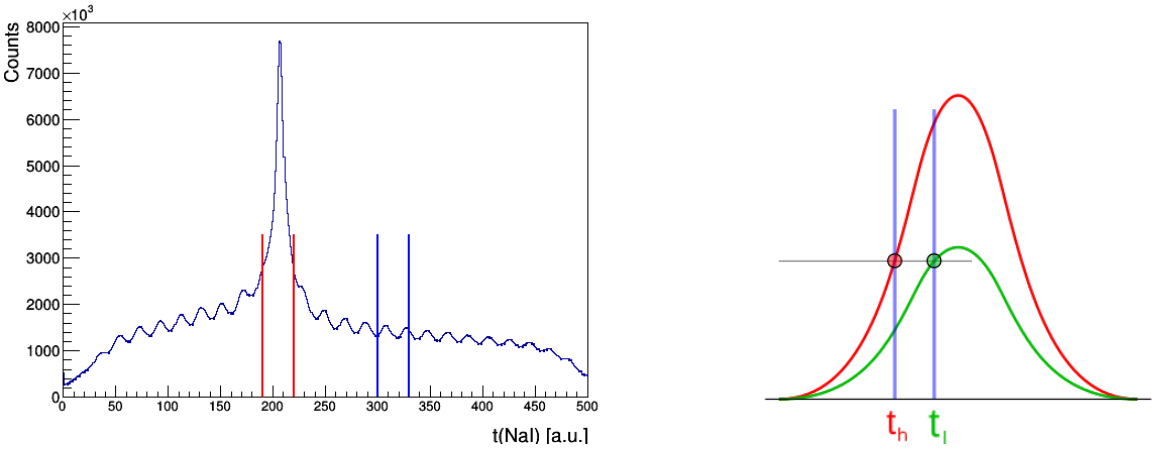

(a) (b)

Figure 2.6.: (a) Time walk corrected time spectrum. The vertical lines indicate the gates set on prompt coincidences (red) and background (blue). (b) Schematic representation of a leading edge discriminator. Signals with larger amplitude have have shorter rise times, thus they trigger earlier. Adopted from [45].

In the data acquisition system the electronic signals that start and stop the TDCs are processed by leading edge discriminators. Signals with larger amplitude, corresponding to

higher energy deposits E, have shorter rise times. This dependence of the signal amplitude on the trigger time t is called time walk and sketched in Figure 2.6b. To correct for this the flowing empirical formula was found [33] and applied to the data

$$t(E) = t_0 + \frac{c_1}{E + c_2} + c_3 \times E, \tag{2.4}$$

where t_0 is the recorded time and c_i are parameters fitted in order to minimize the effect of time walk.

2.4. Particle – γ-ray coincidence matrix

Once all data has been calibrated and the necessary gates have been set, the remaining task is to sort coincidences between protons and γ-rays from the reaction ^{239}Pu(d,p)^{240}Pu. Figure 2.7 displays the excitation energy E_x of the compound nucleus ^{240}Pu (calculated from the kinematic of the reactions), plotted as a function of the coincident γ-ray energies. It highlights characteristic features like the $E_\mathrm{x} = E_\gamma$ diagonal, which results from direct decays to the ground state.

The strong peaks in the coincidence matrix result from reactions with the ^{239}Pu target contaminants like ^{16}O and the ^{9}Be backing. Although they need to be removed in the course of the analysis, at this stage they were used to confirm the excellent quality of the γ-ray calibration.

The horizontal stripes at i.a. $E_\mathrm{x} = 4.6, 5.4$ and $6.6\,\mathrm{MeV}$ occur at the same energies as very strong peaks in the particle spectrum and contain counts with higher γ-ray energies than the excitation energy E_x. This can not be explained by de-excitation of the nucleus, but it is attributed to pile-up in the detectors.

Also given is the neutron separation energy S_n at 6.534 MeV [46] and the (inner) fission barrier E_a at 6.05 MeV [47]. At excitation energies exceeding the respective values, new reaction channels open up and may heavily compete with the de-excitation by gamma emission. Therefore often a drop in the γ-ray intensity is observed.

Figure 2.8 contains the particle – γ-ray events in coincidence with fission. The inset in the lower right corner displays a histogram for the excitation energy E_x. The shape is in good agreement with previous studies for (d,pf)-reactions as shown for example in Figure 3 of Ref. [48]. Tunneling allows fission events at excitation energies E_x below the fission barrier E_a. Note that states in the second well of the barrier can lead to sub-barrier fission resonances [49], which is observable in the a small peak about 1 MeV below the fission barrier of ^{240}Pu. As γ-rays from fission create false coincidences in our data analysis only events below $E_\mathrm{x} < 4\,\mathrm{MeV}$ are used further on.

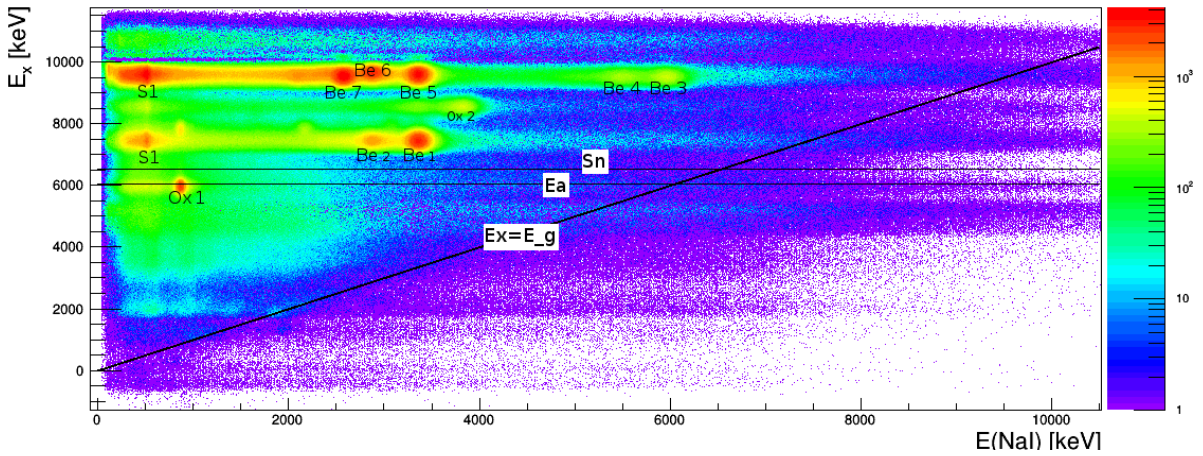

Figure 2.7.: Particle – γ-ray coincidence matrix. The diagonal $E_x = E_\gamma$ highlights direct decays into the ground state and the horizontal line gives the neutron separation energy S_n. The horizontal stripes at i.a. $E_x = 4.6, 5.4$ and $6.6\,\mathrm{MeV}$ are attributed to pile-up in the detectors. Visible peaks due to contaminants are labeled in Table 2.2.

Table 2.2.: Peaks from contaminants in the coincidence matrix and the fitted energies E_{fit} (simple Gaussian, no background subtraction). The error on the fit is estimated to be about ± 20 keV due to the simple fitting procedure. The reference values E_{ref} are taken from from the ENSDF database [43, 44].

Label	Nucleus	E_{fit} [keV]	E_{ref} [keV]	Comment
Ox 1	^{17}O	875	870	1$^{\mathrm{st}}$ ex. level, calibration line
Ox 2	^{17}O	3834	3842	3$^{\mathrm{rd}}$ ex. level
S 1		515	511	annihilation peak
Be 1	^{10}Be	3363	3367	1$^{\mathrm{st}}$ ex. level, calibration line
Be 2	^{10}Be	2867	2856	single escape peak
Be 3	^{10}Be	5965	5956	decay to gs, branching ration 10%
Be 4	^{10}Be	5480	5445	single escape peak
Be 5	^{10}Be	3365	3367	1$^{\mathrm{st}}$ level populated from "Be 7"
Be 6	^{10}Be	2876	2856	single escape peak
Be 7	^{10}Be	2582	2590	decay to 1$^{\mathrm{st}}$ ex. level ($\rightarrow$"Be 5"), branching ratio 90%

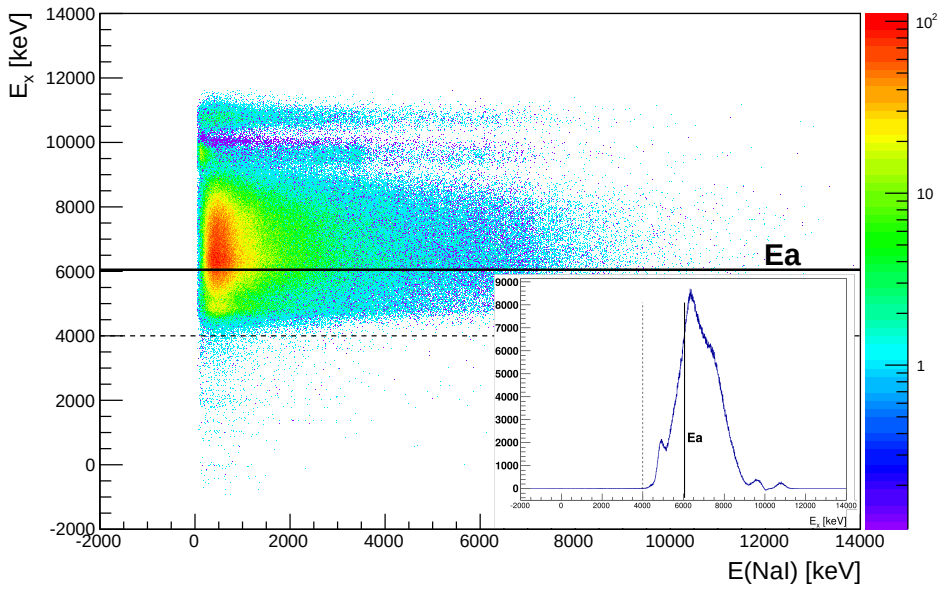

Figure 2.8.: Particle – γ-ray coincidences from fission events. Tunneling allows fission at excitation energies E_{x} below the fission barrier E_a (highlighted). The inset in the lower right corner is a histogram for the excitation energy E_{x}. The small peak about 1 MeV below the fission barrier of ^{240}Pu is attributed sub-barrier fission resonance.

Chapter 3.
3 Data Analysis

"I'm afraid I can't comment on the name Rain God at this present time, and we are calling him an example of a Spontaneous Para-Causal Meteorological Phenomenon."
"Can you tell us what that means?"
"I'm not altogether sure. Let's be straight here. If we find something we can't understand we like to call it something you can't understand, or indeed pronounce.

Douglas Adams
The Hitchhiker's Guide to the Galaxy

This section explains how the level density ρ and the γ-ray strength function γSF are obtained from the particle-γ coincidences. The procedure was established over several years by the nuclear physics group at the University of Oslo and has since become known as the Oslo method. Primary input are the events detected from the ^{239}Pu(d,p)^{240}Pu reaction which were extracted in the previous section. The corresponding γ-ray spectrum needs to be unfolded to correct for the single and double-escape peaks, photon annihilation and the Compton scattering process. From the unfolded spectrum, the primary γ-ray energy distribution is created for each excitation energy. An iterative procedure is applied on this so-called first-generations matrix to find the functional form of the level density ρ and the γ-ray strength function γSF. Finally, information from other experiments is used to normalize the results.

3.1. Unfolding procedure

Photons emitted from an interrogated nucleus interact with matter in various ways. In the first section, the nature and impact of the interactions is briefly characterized. Because these interactions influence how much energy is deposited in the detectors, it is then discussed how unfolding the γ-ray spectrum is used to account for those effects in the analysis. The unfolding and correction method applied to reconstruct the incident spectrum were developed by Guttormsen et al. [50] and are summarized in the following.

In photo-electric absorption the γ-ray transfers all its energy to the detector material, so that one observes a full-energy peak E_γ in the measured energy spectrum. However, the photon can also be scattered and then it transfers a large fraction of its energy to a quasi-free electron (in

the detector material), a process which is called Compton-scattering. The scattering angle θ determines the amount of energy that is transfered to the electron and thus also the γ-ray energy observed in the spectrum. Additionally, the spectrum may contain a low energy peak from backscattered photons absorbed in the detector.

Furthermore, if the γ-ray energy exceeds twice the electron rest mass $m_e \approx 511\,\mathrm{keV}$, pair production in the Coulomb-field of a nucleus can lead to the creation of an electron-positron pair. The positron quickly annihilates with any close-by electron to produce two 511 keV photons. This may cause several peaks in the spectrum. If both annihilation photons are absorbed in the detector, the process contributes to the full-energy peak. However, if one of the photons escapes the detector without being absorbed, this leads to a single-escape peak with $E = E_\gamma - 511\,\mathrm{keV}$. A double-escape peak with $E = E_\gamma - 2 \times 511\,\mathrm{keV}$ is observed when both photons can escape the detector. Additionally, the escape of annihilation photons from pair production in surrounding materials lead to the detection of the so-called annihilation peak at $\approx 511\,\mathrm{keV}$.

The effect of the interactions mentioned above can be expressed by the detector response $\mathbf{R}(E_\gamma, E)$. It describes the probability for a count in the detector (channel) with energy E as a function of the incident γ-ray energy E_γ. It is common practice to denote the original spectrum of incident photons as the unfolded spectrum u. The measured spectrum f is then obtained by folding with the detector response $\mathbf{R}$

$$f = \mathbf{R}u. \tag{3.1}$$

Note that while the procedure follows Guttormsen et al. [50], the response $\mathbf{R}$ for the set-up at OCL was remeasured in 2012 [1]. Thus Table 1 in Ref. [50] has to be replaced by the new values given in the appendix, Table A.1.

To obtain the unfolded spectrum u, the most intuitive method is to invert the response $\mathbf{R}$ and multiply it with f. However, according to Guttormsen et al. [50], this approach leads to strong oscillations in the unfolded spectrum u, due to which the resolution of u appears to be higher than the experimental resolution. They achieved better result with a method which iteratively folds the initially measured spectrum r to obtain the unfolded spectrum u. The folding iteration method consists of the following steps:

1. As we do not know u, the observed spectrum r is set as an initial trial function u^0:
$$u^0 = r. \tag{3.2}$$
2. We calculate the (first) folded spectrum f^i, where i is the iteration index:
$$f^i = \mathbf{R}u^i. \tag{3.3}$$
3. Next, an improved trial function u^{i+1} is obtained by adding the difference $r - f^i$ to the previous trial function u^i:
$$u^{i+1} = u^i + (r - f^i). \tag{3.4}$$
4. After repeating step (2) and (3) about ten times ($i = 10$), the folded spectrum f^{10} reproduces the observed spectrum r within the uncertainties. We have thus found the unfolded spectrum $u \approx u^{10}$. The results are discussed in the next section.

[1] M. Guttormsen (UiO), priv. comm., 03.02.2015.

3.2. Compton subtraction method

The spectrum u gained from the folding iteration method still contains artificial fluctuations. The idea of the Compton subtraction method developed by Guttormsen et al. [50] is to smooth the contribution from Compton scattering, further denoted as the Compton background c, before removing it from the observed spectrum r. This is justified under the assumption that the Compton background varies only slowly as a function of the energy.

First we define a new spectrum v that includes all contribution apart from Compton scattering:

$$v(i) = r(i) - c(i) \tag{3.5}$$
$$= p_{\mathrm{f}}(i)\, u(i) + w(i), \tag{3.6}$$

where i is the channel number, $p_{\mathrm{f}}(i)\, u(i)$ is the *f*ull-energy peak contribution, and the structures due to *s*ingle and *d*ouble escape and the *a*nnihilation peak are summed up in $w = u_{\mathrm{s}} + u_{\mathrm{d}} + u_{\mathrm{a}}$. The three terms are calculated as

$$u_{\mathrm{s}}(i - i_{511}) = p_{\mathrm{s}}(i)\, u(i), \tag{3.7}$$
$$u_{\mathrm{d}}(i - i_{1012}) = p_{\mathrm{d}}(i)\, u(i), \tag{3.8}$$
$$u_{\mathrm{a}}(i_{511}) = \sum_i p_{\mathrm{a}}(i)\, u(i). \tag{3.9}$$

The probabilities p_x in the above formulas are obtained from measurements of mono-energetic γ-transitions and interpolations for values between the corresponding peaks. Furthermore, in the current analysis the spectra u_i are smoothed with 10% of the FWHM measured for the mono-energetic peaks in order to reproduce the energy resolution of the measured spectrum.

In the next step, one can extract the Compton background spectrum c by

$$c(i) = r(i) - v(i). \tag{3.10}$$

The essential aspect of the method is the assumption, that the Compton background c varies only slowly as a function of the energy. Therefore we smooth this spectrum rather strongly (FWHM of corresponding mono-energetic peaks) to suppress the propagation of artificial oscillations to the final spectrum.

At last, the smoothed Compton background c and the structures w are subtracted from the observed spectrum r. Including the probability to obtain a full-energy peak p_{f} and efficiency ϵ_{tot} of the set-up, we finally obtain the (incident) spectrum of full energy peaks U_{full}

$$U_{\mathrm{full}} = \frac{r(i) - c(i) - w(i)}{p_{\mathrm{f}}(i)\, \epsilon_{\mathrm{tot}}(i)}. \tag{3.11}$$

This method can result in a negative number of counts in several bins of the spectrum. This unphysical result is fixed by averaging the values of these channels with those of close-by channels.

Though not a straight forward proof, at least an indication for the capability of the unfolding method including (the Compton subtraction) is given by applying the folding operation $\mathcal{F}$ to the unfolded spectrum u

$$\mathcal{F}(u) \simeq r. \tag{3.12}$$

Equality only holds true for an ideal unfolding procedure. In Figure 3.1 it can be observed that above 150 keV there is no significant deviation between the result of our procedure and the originally observed spectrum r.

The unfolding and Compton subtraction method have been applied to the γ-ray spectra for each excitation energy E_x. The result is shown in Figure 3.2. Additionally, the 870 keV contermination peak from the first excitation level of ^{17}O seen in Fig. 2.7 has been removed by a linear interpolation between the surrounding spectra.

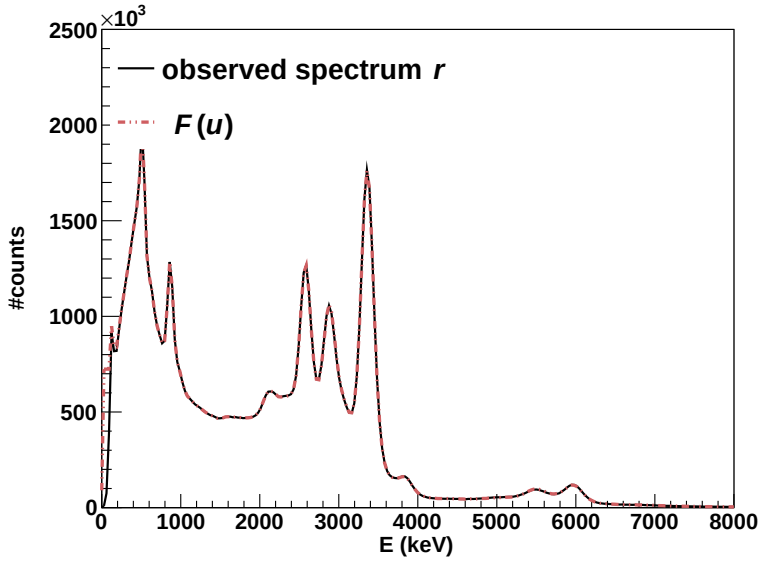

Figure 3.1.: Capability of the unfolding method. Displayed are the detected coincidence γ-ray spectrum r and the folding of the unfolded spectrum $\mathcal{F}(u)$. Above 150 keV there is no significant difference between the two spectra.

3.3. First-generation matrix

When higher excited states decay by γ-ray emission, in general this involves not only direct transitions to the ground-state. The state may decay through intermediate levels emitting a cascade of photons. The first emitted photon in the cascade is called a primary or first-generation γ-ray. The corresponding matrix containing the distribution of these photons for each excitation energy E_x is thus labeled primary γ-ray or first-generations matrix. Since the level density and strength function can be extracted from this matrix, a method has been developed to separate the primary γ-rays from the rest of the cascades. The main features of this method will be outlined in the following, for more information see Guttormsen et al. [51].

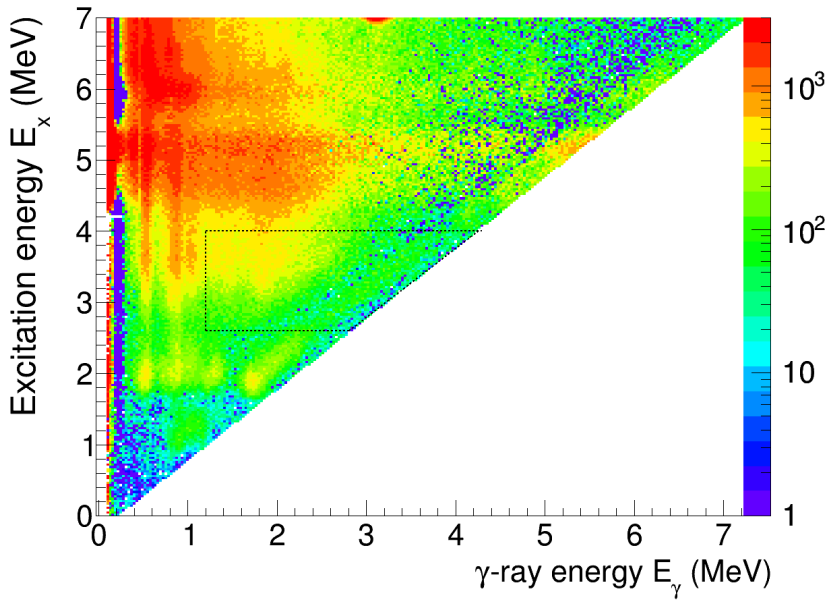

Figure 3.2.: Unfolded coincidence spectrum of particles and γ-rays. The dashed lines indicate the region for the extraction of the level density and strength function (see Section 3.3).

The principal assumption of the first-generation method is that the γ decay from any excited state (more precisely, from any excitation energy bin) is independent of its formation. Thus levels populated by the decay of higher-lying states (bins) have the same decay properties as those populated directly by nuclear reactions. The justification of this assumption is discussed in more detail in Section 3.8.2.

Experimentally we cannot distinguish between the emission time of photons from the same cascade. The only information available from our set-up is the initial excitation E_x from which the cascade originates. However, we can apply an iterative subtraction method that is illustrated in Figure 3.3 to obtain the spectrum of primary γ-rays h_i for each bin i. The idea is that in the unfolded spectra[2] $f_{j<i}$ contain all transitions except the first γ-rays emitted from bin i. Thus, we can obtain the primary γ-ray spectrum h_i by subtracting the spectra $f_{j<i}$ of the lower bins

$$h_i = f_i - g_i, \quad \text{where } g_i = \sum_{j<i} n_{ij} w_{ij} f_j. \tag{3.13}$$

Here w_{ij} is the initially unknown probability for the γ-decay from bin i to bin j (normalized such that $\sum_j w_{ij} = 1$). In other words, w_{ij} gives the branching ratio for decay from the excitation energy bin i and according to our assumption corresponds directly to the primary γ-ray spectrum h_i.

[2] In the previous chapters the folded spectrum was denoted f_i and the unfolded spectrum u_i, respectively. Please note that the notation in the following is adopted to the principal reference for the method [51].

In general, the formation cross section varies between different states. To account for this one introduces the coefficients n_{ij}. They are determined such, that the number of counts for each spectrum f_i when multiplied by n_{ij} results in the same number of cascades.

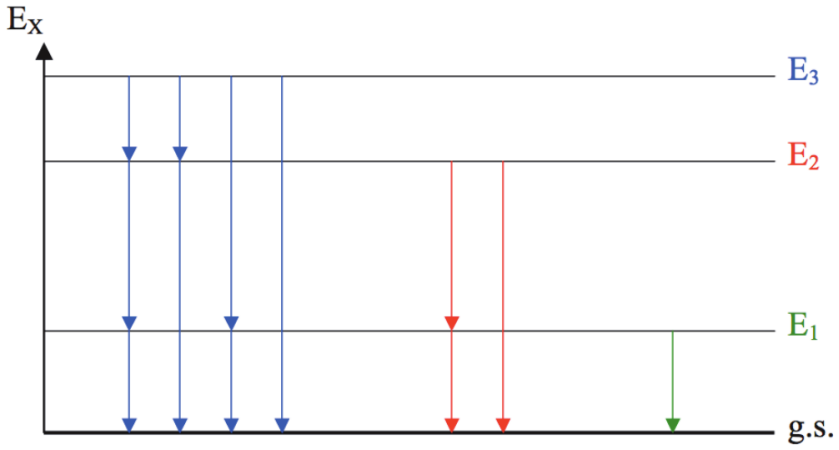

Figure 3.3.: Decay cascades for a hypothetical nucleus. The primary γ-rays from the level E_3 (blue lines) can be obtained by subtracting the spectra from the levels below, E_2 (red line) and E_1 (green lines).

The factors n_{ij} can be determined in following ways:

1. Singles normalization: The single particle spectrum[3] is proportional to the population of each bin, and thus the number of cascades emerging from it. Given the number of counts $S_{i,j}$ for the bins i and j in the single particle spectra, their population ratio is given by

$$n_{ij} = \frac{S_i}{S_j}. \tag{3.14}$$

2. Multiplicity normalization: Equation 3.14 can be expressed in terms of the average γ-ray multiplicity $\langle M_i \rangle$ for the bins i and j. First, we note that the number of counts S_i for a bin in the singles spectrum is equivalent to the number of counts of the spectrum f_i (given by the area $A(f_i)$) divided by the multiplicity $\langle M_i \rangle$

$$S_i = \frac{A(f_i)}{\langle M_i \rangle}. \tag{3.15}$$

The average multiplicity $\langle M_i \rangle$ gives the average number of γ-rays in the decay cascades from bin i. The average energy $\langle E_{\gamma,i} \rangle$ of each of these γ-rays is related to the excitation energy[4] E_i by

$$\langle E_{\gamma,i} \rangle = \frac{E_i}{\langle M_i \rangle}. \tag{3.16}$$

[3]The single particle spectrum corresponds to all (d, p) events, in contrast to the coincident spectrum that requires simultaneous detection of γ-rays. Direct population of the ground-state will, for example, only be seen in the singles spectrum.

[4]In the following, the index x is dropped from the excitation energy $E_{x,i}$ for bin i to avoid an overload of the notation . It should still be easily destinguishable from the γ-ray energy E_γ.

We can rearrange this equation to calculate the average multiplicity $\langle M_i \rangle$ for each bin

$$\langle M_i \rangle = \frac{E_i}{\langle E_{\gamma,i} \rangle}. \tag{3.17}$$

Combining Equation (3.14) to (3.17) we obtain following expression for the correction factors n_{ij} when subtracting bin j from bin i

$$n_{ij} = \frac{A(f_i)/\langle M_i \rangle}{A(f_j)/\langle M_j \rangle} = \frac{A(f_i)\langle E_{\gamma,i} \rangle}{A(f_j)\langle E_{\gamma,j} \rangle} \frac{E_j}{E_i}. \tag{3.18}$$

The two normalization methods have been shown to lead to the same results within the experimental uncertainties [12] for most nuclei. In this analysis we chose the second method, as it is assumed to be more robust[5].

The number of counts in the primary γ-ray spectrum $A(h_i)$ should be equal to the counts in the unfolded spectrum $A(f_i)$ minus the counts in the underlying spectra $A(g_i)$. An improper choice of the weighting functions w_{ij} may violate this relation. It can be corrected introducing a parameter δ, close to unity, and substituting $A(g_i)$ by $\delta A(g_i)$. Then we find the following two alternative descriptions for the counts in the primary γ-ray spectrum $A(h_i)$

$$A(h_i) = A(f_i) - \delta A(g_i), \tag{3.19}$$

$$A(h_i) = \frac{A(f_i)}{\langle M_j \rangle}, \tag{3.20}$$

which we can solve for δ,

$$\delta = \left(1 - \frac{1}{\langle M_j \rangle}\right) \frac{A(f_i)}{A(g_i)}. \tag{3.21}$$

The parameter δ is varied in order to obtain the best agreement between the number of counts in h_i, f_i and g_i. If the necessary variation exceeds $\delta = 15\%$, a new weighting function should be tried instead.

We have now explored all tools that form the iterative procedure which we use to extract the first-generation spectrum h_i:

1. Apply a trial function w_{ij}. The choice for the initial function in this work has been a primary γ-ray spectrum as expected from the a Fermi gas model.
2. Calculate h_i.
3. Transform h_i to w_{ij} by application of the same energy calibration and normalization of $A(h_i)$ to unity.

[5] An example taken from Ref. [12] are isomeric states with lifetimes greater than the TDC gate that pose a problem to the singles normalization. Photons from these states are not registered in coincidence with the particle spectra. The number of counts in the singles spectrum in that case doesn't correspond to the number of gammas from the state anymore. The multiplicity can still be determined by Eq. (3.17), as the average γ-ray energy will not change drastically.

4. The result from step 3 can be used as new input for step 2. Convergence is reached if $w_{ij}^{\text{new}} \approx w_{ij}^{\text{old}}$.

The convergence properties have been tested and the results are in good agreement with simulated spectra already after three iterations. For this analysis 10 - 20 iterations are performed for each spectrum f_i. Combining the results for each excitation energy bin i, the first-generations matrix for this experiment is shown in Figure 3.4 (a). The γ-rays below 1.2 MeV were excluded, as there are several strong transitions, e.g. the annihilation peak, that could not be subtracted properly.

An additional correction was applied to the first-generations matrix. The feature was first explained by Larsen et al. [12] and is briefly discussed in the following.

The direct reaction cross-section has a strong dependence on the intrinsic wave functions of lower-lying states. Therefore, it is possible that some of these states have a high (d, p) cross-sections, whilst being only weakly populated through decay from higher-lying states. The procedure above would then lead to subtraction of too many γ-rays from the lower states, observable by a vertical valley of low counts in the first-generations matrix. As can be seen from Figure 3.4 (a), the initial first-generations matrix exhibits such valleys at around $E_\gamma \approx 1.1\,\text{MeV}$ and $E_\gamma \approx 1.7\,\text{MeV}$. To compensate for this effect, we excluded this low-lying states by artificially setting their weighing functions w_{ij} to 0. The final first-generations matrix including these corrections is displayed in Figure 3.4 (b).

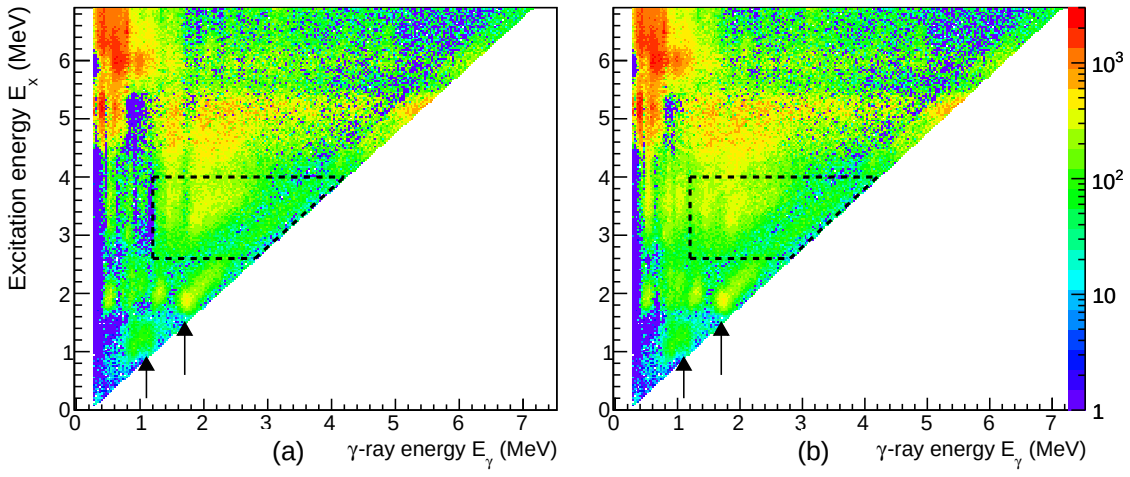

Figure 3.4.: First-generations matrix. The arrows point at vertical valleys of low counts in the initial matrix (a) that have been compensated in (b) (most easily visible at $E_\gamma \approx 1.1$MeV). The dashed lines indicate the energy region for the extraction of the level density and strength function.

In the following, the analysis will be constrained to energies between $(E_\text{x}^\text{min}, E_\text{x}^\text{max}, E_\gamma^\text{min}) = (2.6, 4.03, 1.2)\,\text{MeV}$. The limits are set in order to utilize only the region of statistical γ-ray transitions and exclude, for example, yrast transitions, as they might be not properly subtracted in the first-generations method. For the upper limit of the excitation energy we need to stay below the neutron separation threshold S_n and in particular also below the set-in of fission events to remain selective on the (n, γ) decay-channel.

3.4. Determining level density and γ-strength function

Up to now the primary γ-ray spectra for each excitation energy (or corresponding bin E_i) have been obtained. They form the first-generations matrix $P(E_i, E_\gamma)$. According to Fermi's golden rule, the decay rate λ_{if} from an inital state $|\mathrm{i}\rangle$ to a final state $|\mathrm{f}\rangle$ (which correspond to $P(E_i, E_\gamma)$) can be decomposed into the transition matrix element, and the level density $\rho(E_\mathrm{f})$ of the final state $E_\mathrm{f} = E_i - E_\gamma$,

$$\lambda_{\mathrm{if}} = \frac{2\pi}{\hbar}|\langle \mathrm{f}|\hat{H}|\mathrm{i}\rangle|^2 \rho(E_\mathrm{f}), \tag{3.22}$$

where $\hat{H}$ is the transition operator. In the regime of statistical γ-rays we need to consider ensembles of initial and final states, thus receiving decay properties averaged over many levels. The principal assumption is the validity of the generalized Brink-Axel hypothesis [52, 53], which states that the Giant Dipole Resonance is build the same way on ground and excited states. Thus the decay properties do not depend on the specific levels, but only the energy difference between them. In a generalized version, this applies for all collective decay modes. Consequently, we can reduce the dependence of the matrix element $\langle \mathrm{f}|\hat{H}|\mathrm{i}\rangle$ on initial and final states to a single dependence on the energy difference given by the γ-ray energy E_γ. The decay probability, corresponding to $P(E_i, E_\gamma)$, can therefore be factorized in the level density $\rho(E_\mathrm{f})$ of the final state and the transmission coefficient $\mathscr{T}(E_\gamma)$,

$$P(E_i, E_\gamma) \propto \rho(E_\mathrm{f})\mathscr{T}(E_\gamma). \tag{3.23}$$

This relation holds true for compound states, where the relative decay probability for each decay channel is independent of the mode of formation [7]. The Brink hypothesis, is believed to be fulfilled at the considered energy regions (see Section 3.8 for more details.). For considerably high excitations ($\approx$ 20MeV) and/or spins involved in a reaction, the Brink hypothesis is violated (for examples, see Ref. [11]).

The basic idea on how to obtain the level density ρ and transmission coefficient $\mathscr{T}$ from $P(E_i, E_\gamma)$ was first presented by Henden et al. [54], whilst the first attempt for an iterative method was given by Tveter et al. [55]. It was improved by Schiller et al. [11] in 2000 to yield the first comprehensive and successful solution. The main steps are outlined in the following.

The procedure is based on a comparison between the first-generations matrix $P(E_i, E_\gamma)$ and a calculated solution $P_{\mathrm{th}}(E_i, E_\gamma)$

$$P_{\mathrm{th}}(E_i, E_\gamma) = \frac{\rho(E_i - E_\gamma)\mathscr{T}(E_\gamma)}{\sum_{E_\gamma = E_\gamma^{\min}}^{E_i} \rho(E_i - E_\gamma)\mathscr{T}(E_\gamma)}, \tag{3.24}$$

where the sum runs within the limits $(E_\gamma^{\min}, E_\gamma^{\max})$ chosen for the experimental matrix $P(E_i, E_\gamma)$. We obtain $P_{\mathrm{th}}(E_i, E_\gamma)$ by iteratively improving the choice of ρ and $\mathscr{T}$ with respect to a χ^2 minimization

$$\chi^2 = \frac{1}{N_{\mathrm{free}}} \sum_{E_i = E_\mathrm{x}^{\min}}^{E_\mathrm{x}^{\max}} \sum_{E_\gamma = E_\gamma^{\min}}^{E_i} \left(\frac{P_{\mathrm{th}}(E_i, E_\gamma) - P(E_i, E_\gamma)}{\Delta P(E_i, E_\gamma)} \right)^2, \tag{3.25}$$

where N_{free} is the number of degrees of freedom (connected to the total number of entries in P, ρ and $\mathscr{T}$), and $\Delta P(E_i, E_\gamma)$ is the uncertainty in the experimental first-generations matrix. For details on the iteration procedure, see Ref. [11].

The results of this procedure are displayed in Figure 3.5 together with the experiential data. In general, there is a good agreement between the fitted and the experimental values.

However, it has also been shown that this method determines only the functional form of the level density ρ and transmission coefficient $\mathscr{T}$ [11]. The following section will treat the correct normalization for these quantities, as identical matrices P_{th} are found for any transformation with parameters α, A and B of the type

$$\tilde{\rho}(E_i - E_\gamma) = A \exp[\alpha\,(E_i - E_\gamma)]\,\rho(E_i - E_\gamma), \tag{3.26}$$

$$\tilde{\mathscr{T}}(E_\gamma) = B \exp[\alpha\,E_\gamma]\,\mathscr{T}(E_\gamma). \tag{3.27}$$

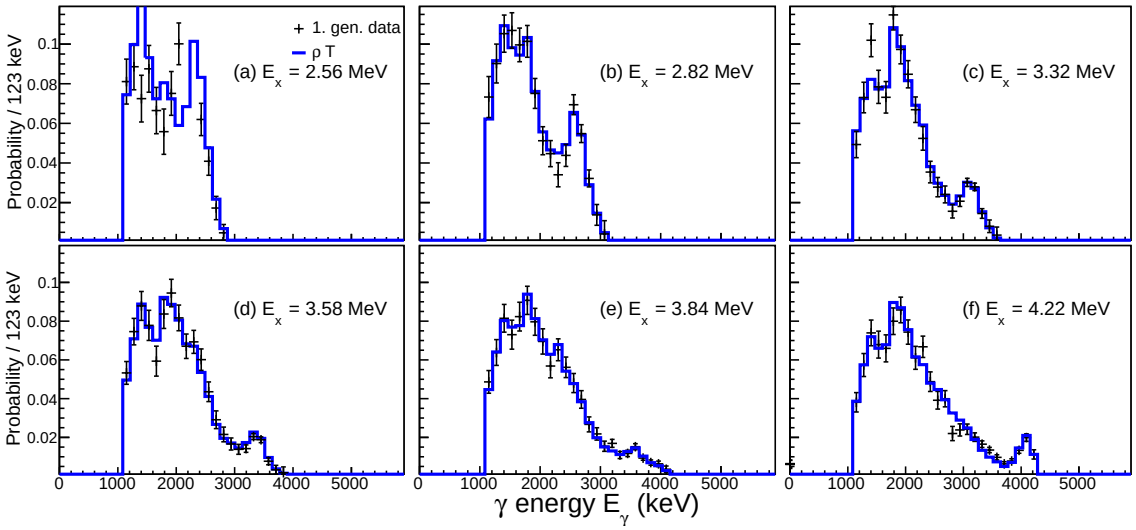

Figure 3.5.: The first-generations spectra for several initial excitation energies E_{x} (crosses) compared to the product of the obtained level density $\rho(E_{\mathrm{f}})$ and transmission coefficient $\mathscr{T}(E_\gamma)$ (blue line). In general, there is a good agreement the fitted and the experimental values.

3.5. Normalizing the level density

In order to determine the transformation parameters α and A in Eq. (3.26) and (3.27) that correspond to the correct physical solution, we need (at least) two normalization points for the level density. At low excitation energies the number of known discrete levels [56] is averaged over 128 keV bins and used up to a cut-off energy where we assume the level scheme to be complete[6]. At high energies we utilize neutron resonance data from (n,γ) reactions. For the latter, the level density at the neutron separation energy $\rho(S_n)$ is calculated under the

[6] We assume that the real level density does not flatten out and the observed plateau at excitations greater than 1 MeV are a manifestation of an incomplete level sceme. This is lower than the calculations in RIPL3, where maximum energy of the still complete level scheme is calculated to be 1.4 MeV [19].

assumption of equal parity from the average neutron resonance spacing for s-waves D_0 taken from RIPL-3 [19] following [11],

$$\rho(S_n) = \frac{2\sigma^2}{D_0} \frac{1}{(I+0)\exp[-(I+1)^2/2\sigma^2] + \exp[-I^2/2\sigma^2]}. \tag{3.28}$$

Here I is the spin of the target nucleus (^{239}Pu). The derivation of any equation relating $\rho(S_n)$ and D_0 is inevitably model-dependent, here using the spin distribution $g(E_\mathrm{x}, I)$ of Gilbert and Cameron [57] together with the rigid-body moment of inertia approach for the spin cut-off parameter σ from 2005 by von Egidy and Bucurescu [58]:

$$g(E_\mathrm{x}, I) = \frac{2I+1}{2\sigma^2(E_\mathrm{x})} \exp[-(I+1/2)^2/2\sigma^2], \tag{3.29}$$

$$\sigma^2(E_\mathrm{x}) = 0.0146A^{2/3} \frac{1+\sqrt{4aU(E_\mathrm{x})}}{2a}, \tag{3.30}$$

where A is the mass number of the nucleus, a is the level density parameter, $U(E_\mathrm{x}) = E_\mathrm{x} - E_1$ is the intrinsic excitation energy, and E_1 is the back-shift parameter. The parameters a and E_1 are taken from the systematic study of Ref. [58]. Table 3.1 lists the adopted values used in the normalization procedure. The effect of different choices for the spin cut-off parameter σ are discussed in Section 3.8.5.

Since there is a gap of about 2.5 MeV between the highest excitation energy of extracted the level densities and the binding energy S_n, an interpolation is used to connect the data. In accordance with the findings for other actinides [13], this is performed under the assumption of a constant temperature level density formula [57]

$$\rho_\mathrm{CT}(E_\mathrm{x}) = \frac{1}{T_\mathrm{CT}} \exp \frac{E_\mathrm{x} - E_0}{T_\mathrm{CT}}, \tag{3.31}$$

with the shift in excitation energy E_0 given by

$$E_0 = S_n - T_\mathrm{CT} \ln[\rho(S_n) T_\mathrm{CT}]. \tag{3.32}$$

The best fit is obtained for a constant temperature of $T_\mathrm{CT} = 0.425(10)$ MeV. The level density obtained with this procedure is shown in Figure 3.6.

3.6. Normalizing the γ-ray strength function

Although we obtain the total level density ρ through normalization, previous analyses in the actinide region [14, 16] suggest that the light ion (d, p) reaction used in this experiment may not transfer enough spin to populate all available levels. This would in general influence the primary gamma ray spectra $P(E, E_\gamma)$, which according to Eq. (3.23) is fitted by the product $\rho(E_\mathrm{f})\mathscr{T}(E_\gamma)$. Following the generalized Brink-Axel hypothesis [52, 53], the transmission coefficient is assumed to be approximately independent of the spin. However, to account for the not populated levels, the observed spectra $P(E, E_\gamma)$ should be fitted with a reduced level density ρ_red instead,

$$P(E, E_\gamma) = \rho(E_\mathrm{f})\mathscr{T}(E_\gamma) \quad \longrightarrow \quad P(E, E_\gamma) = \rho_\mathrm{red}(E_\mathrm{f})\mathscr{T}(E_\gamma). \tag{3.33}$$

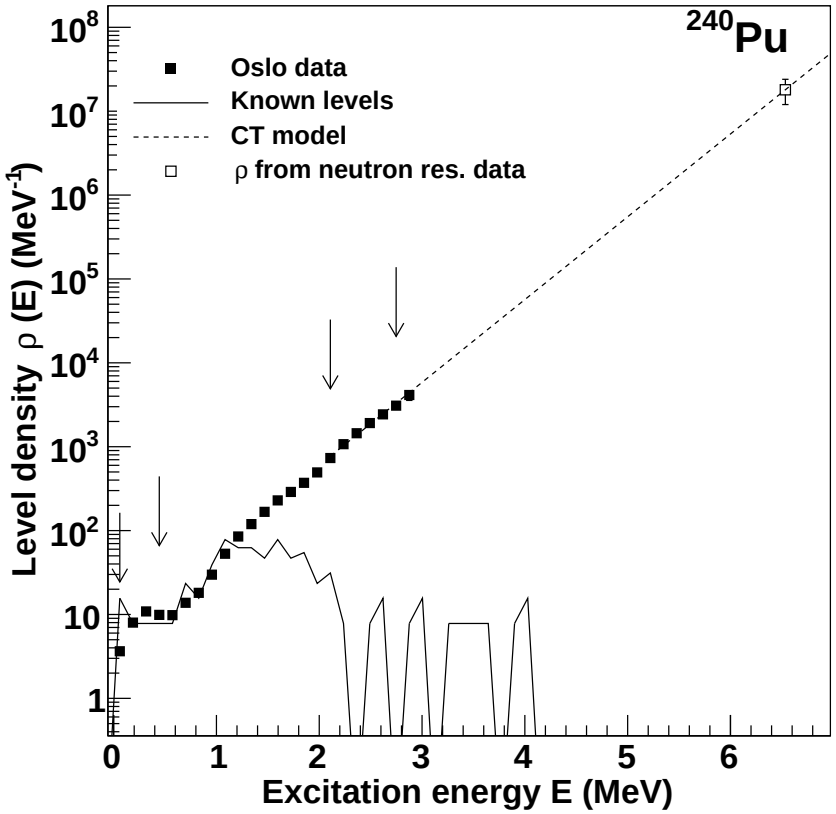

Figure 3.6.: Level density obtained with the Oslo method. The experimental data is normalized to known discrete levels at lower excitation energies taking into account the level scheme up to where it is assumed to be complete. The level density at the neutron separation energy $\rho(S_n)$ is calculated from the neutron resonance spacing D_0. Between the last data points and the separation energy an interpolation with a constant temperature level density formula with $T_{\mathrm{CT}} = 0.425(10)\,\mathrm{MeV}$ is applied.

Table 3.1.: Parameters used to extract level density and γ-strength function (see text). Where applicable, references are stated next to the variable.

S_n [46] [MeV]	a [58] [MeV^{-1}]	E_1 [58] [MeV]	$\sigma(S_n)$	D_0 [19] [eV]	$\rho(S_n)$ [$10^6\,\mathrm{MeV}^{-1}$]	$\rho(S_n)_{\mathrm{red}}$ [$10^6\,\mathrm{MeV}^{-1}$]	T_{CT} [MeV]	$T_{\mathrm{CT},\rho_{\mathrm{red}}}$ [MeV]	$\langle\Gamma_\gamma(S_n)\rangle$ [19] [MeV]
6.53420(23)	25.16(20)	0.12(8)	8.43(80)	2.20(9)	32.7(66)	18	0.425(10)	0.44(1)	43(4)

Although the exact form of the reduced level density ρ_{red} needs to be investigated further, the simplest working hypothesis[7] is that for each excitation energy only a fraction dependent on a parameter $r < 1$ of all levels is populated. In the constant temperature interpolation Eq. (3.31) one has to replace the total level density ρ_{tot} by

$$\rho_{\mathrm{red}}(S_n) = r\rho_{\mathrm{tot}}(S_n). \tag{3.34}$$

The parameter r is chosen within the range of previous analyses [14, 16], and such that resulting transmission coefficient fits smoothly to existing data from other experiments. This is discussed in more detail in the following section.

With this pretext we can now attempt to find the correct normalization for the transmission coefficient $\mathscr{T}$. One of the two parameters in the transformation, Eq. (3.27), was already determined. Now we use literature values of the average total radiative width $\langle\Gamma_\gamma\rangle$ at the neutron separation energy S_n to obtain the second parameter B. Assuming that the γ-decay is dominated by dipole transitions and that equal parity holds for all excitation energies and spins, one finds [11, 59]

$$\langle\Gamma_\gamma(S_n)\rangle = \frac{1}{2\pi\rho(S_n, I, \pi)} \sum_{I_f} \int_0^{S_n} dE_\gamma \, B\mathscr{T}(E_\gamma)\rho_{\mathrm{tot}}(S_n - E_\gamma, I_f). \tag{3.35}$$

Here the summation runs over all final levels with spin I_f accessible though γ-transitions with energy E_γ, and the initial spin and parity are denoted by I and π. Note that the total level density ρ_{tot} is used, as the reduced spin distribution has already been accounted for in the extraction of the transmission coefficient $\mathscr{T}$. Again, the spin distribution $g(E_{\mathrm{x}}, I)$ of Ref. [57] together with the spin cut-off parameter σ by von Egidy and Bucurescu [58] from 2006 was implied in the derivations; a more detailed account can be found in Ref. [37].

Due to the uncertainty of the exact form and reduction of the level density, the determination of the parameter α through ρ_{red} in Eq. (3.26) becomes rather unreliable. Thus we proceed in inverse order and first compare our results (after conversion to the γ-ray strength function) with extrapolations from photo-nuclear experiments in order to then find the correct normalization.

The γ-ray strength function $f(E_\gamma)$ (in the following abbreviated as γSF) is a measure of the transition probability between states. It emerges naturally from a quantum mechanical treatment of transitions between states. It can be shown that when a multipole expansion is applied, the transition probability is directly dependent on the energy difference between states and the order of the expansion, that is $L = 1$ for dipole, $L = 2$ for quadrupole radiation, etc., see Ref. [7, p.595]. The γSF is defined such that it divides out this direct energy dependence of the transmission coefficient $\mathscr{T}(E_\gamma)$, thus one remains with the "strength" of the transition.

$$f(E_\gamma) = \frac{1}{2\pi}\frac{\mathscr{T}(E_\gamma)}{E_\gamma^{2L+1}} \overset{\substack{\mathrm{L=1}\\ \mathrm{transition}}}{=} \frac{1}{2\pi}\frac{\mathscr{T}(E_\gamma)}{E_\gamma^3}. \tag{3.36}$$

Figure 3.7 shows the comparison to the strength function obtained from photo-nuclear reaction cross-sections $\sigma_{\gamma,\mathrm{abs}}$, where we used the following relation to convert the latter [60]:

$$f(E_\gamma) = \frac{1}{3\pi\hbar^2c^2}\frac{\sigma_{\gamma,\mathrm{abs}}}{E_\gamma}. \tag{3.37}$$

[7] This hypothesis has the beauty of introducing only a single parameter, which could potentially be calculated using nuclear reaction codes. A drawback is that the level density at low excitation energies is also reduced, even though here one expects spins reachable even by a low spin transfer.

To our knowledge there are no published measurements on ^{240}Pu. We assume that the cross-sections for neighboring nuclei in this mass region do not show strong variations and thus apply photo-nuclear data for ^{239}Pu. The comparison includes the γSF derived from (γ, x) (also called (γ, abs)) cross-sections by Gurevich et al. [61], Caldwell et al. [62] and De Moraes and Cesar [63].

As our data covers γ energies below the neutron separation energy S_n, the (γ, x) data needs to be extrapolated to lower energies. The clearly visible double-humped structure of the Giant Electric Dipole Resonance (GEDR) is fitted with two enhanced generalized Lorentzians (EGLOs) as defined in Eq. (A.2). The most recent measurements, performed by De Moraes and Cesar [63], give strong indications of a resonance-like structure[8] at around 7.5 MeV, that was previously postulated for other actinides [14, 16]. It has been fitted with a standard Lorentzian (SLO) given in Eq. (A.1) and is labeled pygmy in Figure 3.7. The sum of these resonances is the estimation for the underlying strength of the γSF (without the scissors-resonance) for our data and is marked with a red line. The resonance parameters for the extrapolation are given in Table 3.2.

The α parameter is adjusted to fit the slope of this estimation; within certain limits, different fits are possible and the resulting uncertainties will be discussed further in Section 3.8.5. Although strictly speaking in the present case it might not have been necessary to reduce the level density, it was nevertheless chosen to follow this procedure in the spirit of previous indications in the actinide region [14, 16]. As a result, the level density at the neutron separation energy S_n was reduced from 32.7×10^6 to 18×10^6 levels per MeV to account for the reduced angular momentum transfer of the (d, p) reaction. Finally, the second parameter B is determined by Eq. (3.35).

3.7. Scissors resonance

Provided that the extrapolation in the previous section is reliable, it can be assumed to be a "baseline" of the γSF. In Figure 3.8 this baseline was subtracted. The observed excess strength is interpreted as the scissors resonance, which is in accordance with previous observations for $^{231-233}$Th, $^{232-233}$Pa, $^{237-239}$U and ^{238}Np [14, 16].

The scissors resonance appears to be split into two components, each of them is fitted with a SLO. The drop in the data points between 1.6 to 1.9 MeV is assumed to be linked to a very strong peak in the coincidence-matrix, that could not be sufficiently accounted for by the "valley"-correction introduced in Section 3.3 on the primary γ-ray extraction procedure.

The strength of each component can be expressed by the relation [14]

$$B_{\mathrm{SR},i} = \frac{9\hbar c}{32\pi^2} \left(\frac{\sigma_{\mathrm{SR},i}\Gamma_{\mathrm{SR},i}}{\omega_{\mathrm{SR},i}} \right). \tag{3.38}$$

[8] The nature and origin of this resonance are not relevant for this analysis and shall thus not be speculated upon.

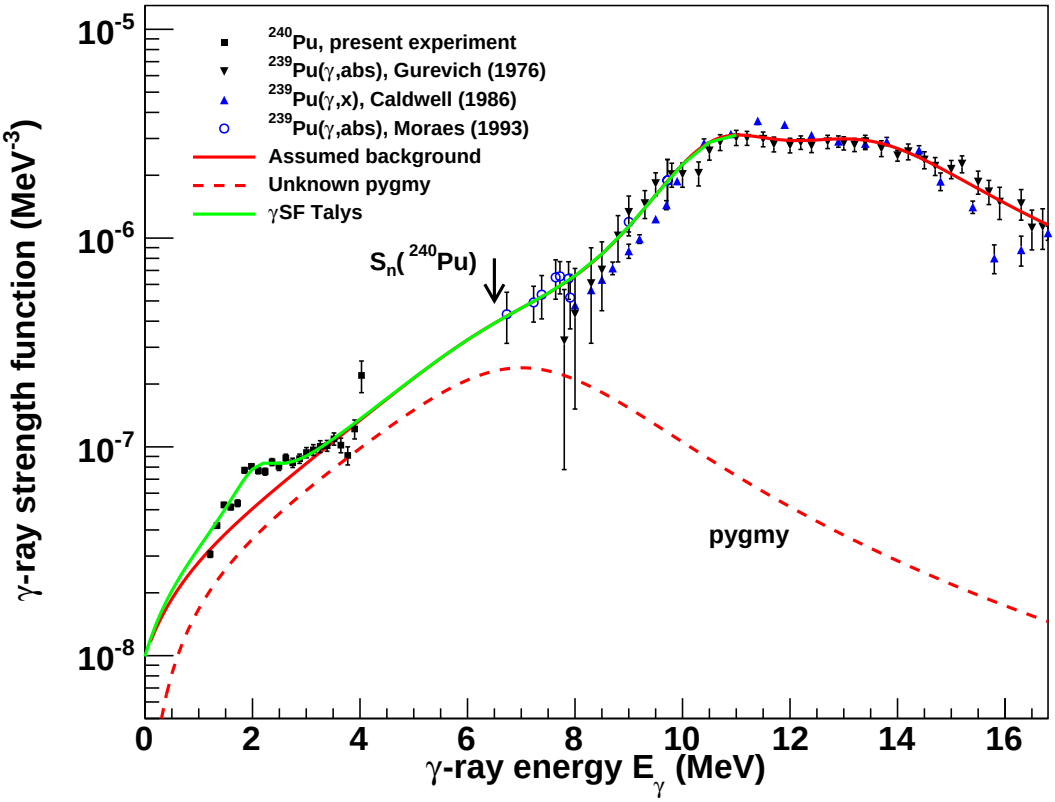

Figure 3.7.: Comparison of the γSF from the present experiment with photoabsorption data by Gurevich et al. [61], Caldwell et al. [62] and De Moraes and Cesar [63]. The solid red line represents the estimated strength without the scissors resonance. The adopted data for further calculations with TALYS [25] is shown with the solid blue line (and mostly falls together with the red line). The dashed red curve is an unknown pygmy resonance introduced to take into account the increased strength at $E_\gamma \approx 7.5\,\mathrm{MeV}$.

Table 3.2.: Parameters used for the γSF extrapolation. The GEDR parameters are indexed $E1,1$ and $E1,2$.

$\omega_{E1,1}$ [MeV]	$\sigma_{E1,1}$ [mb]	$\Gamma_{E1,1}$ [MeV]	$\omega_{E1,2}$ [MeV]	$\sigma_{E1,2}$ [mb]	$\Gamma_{E1,2}$ [MeV]	T_f [MeV]	ω_{pyg} [MeV]	σ_{pyg} [mb]	Γ_{pyg} [MeV]
11.3	290	3.2	14.15	340	5.5	0.34	7.5	20	5.45

[9]The quadrupole deformation parameter δ is in first order related to ϵ_2 and β_2 by $\delta \approx \epsilon_2 \approx \beta_2\sqrt{45/(16\pi)}$.

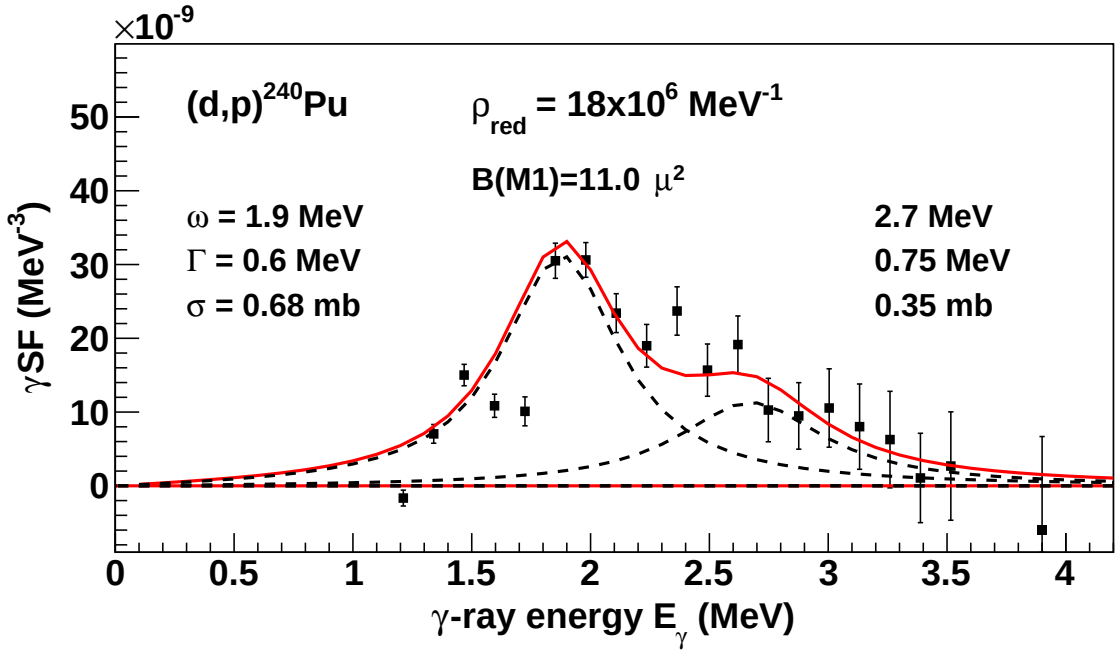

Figure 3.8.: The extracted scissors resonance. It is fitted with two SLO resonances (dashed lines) and the parameters are given in the plot. The resulting strength is $B(M1) \approx 11\mu_N^2$. The drop in the data points between 1.6 to 1.9 MeV is assumed to be linked to a very strong peak in the coincidence-matrix, that could not be sufficiently accounted for in the primary γ-ray extraction procedure.

Table 3.3.: Parameters of the scissors resonance and the sum-rule estimates. The deformation parameter[9] $\delta = 0.274$ which has been taken from RIPL3 [19] is applied in the sum rule

Lower resonance				Upper resonance				Total		Sum rule	
$\omega_{SR,1}$ [MeV]	$\sigma_{SR,1}$ [mb]	$\Gamma_{SR,1}$ [MeV]	$B_{SR,1}$ [μ_N^2]	$\omega_{SR,2}$ [MeV]	$\sigma_{SR,2}$ [mb]	$\Gamma_{SR,2}$ [MeV]	$B_{SR,1}$ [μ_N^2]	ω_{SR} [MeV]	B_{SR} [μ_N^2]	ω_{SR} [MeV]	B_{SR} [μ_N^2]
1.90(05)	0.68(5)	0.60(10)	7.6(14)	2.70(10)	0.35(5)	0.75(15)	3.4(9)	2.15(6)	11.0(16)	2.24	10.1

Table 3.3 lists resonance parameters for both components together with the total strength B_{SR} and average energy centroid ω_{SR}, which are calculated by [14]

$$B_{\mathrm{SR}} = \sum_{i=1,2} B_{\mathrm{SR},i}, \tag{3.39}$$

$$\omega_{\mathrm{SR}} = \frac{\sum_{i=1,2} \omega_{\mathrm{SR},i} B_{\mathrm{SR},i}}{\sum_{i=1,2} B_{\mathrm{SR},i}}. \tag{3.40}$$

The statistical uncertainty is estimated by linear error propagation following a one by one variation of the resonance parameters ω, σ and Γ within reasonable limits. As a comparison we also estimate the parameters by the sum rule [64]. The calculations follow the derivation of Enders et al. [65], however the ground-state moment of inertia is replaced by a rigid-body moment of inertia. The resulting description and formulas for the quasi-continuum can be found in Ref. [14]; here it shall only be noted that the resulting $B(M1)$ value is proportional to the moment of inertia Θ. There is a reasonably good agreement between the sum rule estimates and the results from this experiment.

The two components of the scissors mode are separated by $\Delta\omega_{\mathrm{SR}} = 0.8(1)\,\mathrm{MeV}$. This is very similar to previous results for ^{243}Pu with $\Delta\omega_{\mathrm{SR}} = 0.81(6)\,\mathrm{MeV}$ [17] and the average of the analyzed Th, Pa and U isotopes $\Delta\omega_{\mathrm{SR}} = 0.89(15)\,\mathrm{MeV}$ [14], but a little higher than for ^{238}Np with $\Delta\omega_{\mathrm{SR}} = 0.53(6)\,\mathrm{MeV}$ [16].

3.8. Systematic errors

I don't know half of you half as well as I should like; and I like less than half of you half as well as you deserve.

J.R.R. Tolkien
The Fellowship of the Ring

In recent years there has been a strong focus on determining and quantifying errors in the Oslo method. As we study experimental data with sufficiently high statistics and therefore low statistical errors, we are most concerned about systematic errors. More information about the estimation and propagation of the statistical uncertainty can be found in Ref. [11]. This section first summaries findings of an article by Larsen et al. [12] on the "Analysis of possible systematic errors in the Oslo method". It investigates the influence of experimental limitations as well as the correctness and impact of assumptions that we applied throughout the analysis. Finally we present the results of a re-analysis of the current data that take into account the most important sources of systematic errors.

At many points the study of Larsen et al. [12] utilizes the DICEBOX code [66]. This algorithm generates the decay scheme of an artificial nucleus from a specified discrete level scheme, level density model and γSF. From this one can create particle-γ coincidences. The uncertainty that an element of the Oslo method generates can be derived from applying the method on the artificial coincidence matrix and comparing the results to the (by definition) correct input models.

3.8.1. Unfolding

The unfolding of the recorded spectrum strongly relies on the correct response matrix of the detector. An error in the total absorption efficiency of the NaI crystals will propagate though the whole method. Thus the consequences of variations of up to $\approx 20\,\%$ for γ-energies above 1 MeV have been simulated with DICEBOX [66]. The study finds that whilst this has almost no effect on the level density, it can considerably change the slope of the γ-ray strength function. The quantitative effect corresponds directly to the imposed variation of the NaI efficiency, which is assumed to be known within about $10\,\%$[10].

3.8.2. First-generations method

The principal assumption in the extraction of the primary γ-rays is that the γ decay from any excited level is independent of the formation of this state. Thus states populated by the decay of higher-lying states have the same decay properties as those populated directly by nuclear reactions. To test the assumption, it is sufficient to check that any level has the same probability to be populated by the two processes, as the branching and decay ratios are properties of the level itself. Looking at how the method is applied, we can (without loss of generality) simply test the hypothesis for each energy bin (instead of each level), thus averaging over many levels and corresponding spins.

In the region of high level densities, as given for actinides above about 1 to 2 MeV, a nucleus bombarded with a light particle seems to thermalize prior to the emission of a γ-ray. In these cases one also speaks of the formation of a compound nucleus. The assumption of a compound reaction is in very good agreement with calculations for ^{160}Dy(^{3}He, $\alpha\gamma$) by Běták [67], which are based on the an inclusion of γ-ray emissions in the pre-equilibrium model[11]. The fraction of γ-rays that do not stem from a compound state is very small for γ-ray energies below $\approx 10\,\mathrm{MeV}$.

Another approach is to compare results derived from two reactions for the same compound nucleus like $^A Z(^3\mathrm{He}, \alpha)^{A-1} Z$ and $^A Z(^3\mathrm{He},^3\mathrm{He}')^A Z$. Examples that have been studied include ^{96,97}Mo [69], ^{161,162}Dy [70] and ^{171,172}Yb [71]. For the energies of interest here there was no significant difference between the obtained level densities and strength functions.

An additional concern for the first-generations method is the variation in the populated spins as a function of the excitation energy. The most significant example which leads to "valleys" in the first-generations matrix has already been mentioned in Section 3.3. The direct reaction cross-section has a strong dependence on the intrinsic wave functions of lower-lying states. Thus it is possible that some levels are strongly fed in the (d, p) reaction, but only weakly populated through decay from higher-lying states. In the applied extraction procedure for primary γ-rays this leads to an erroneously high subtraction of γ-rays from the lower states, observable by a vertical valley of low counts in the first-generations matrix.

Besides the influence of the finite detector resolution and the difference between the normalization options have been studied with spectra created through the DICEBOX code [66]. It is found to be much smaller than the statistical errors.

[10] M. Guttormsen (UiO), priv. comm., 30.09.2015.

[11] This model bridges the gap between calculations that rely only on either compound or direct reactions. The determination of the direct component is important in this case, because it is characterized by a strong correlation between formation and decay channel. For an introduction to the model, see Ref. [68].

3.8.3. Brink-Axel hypothesis

We determine the level density ρ and γ-ray transmission coefficient $\mathscr{T}$ under the assumption that the generalized Brink-Axel hypothesis holds true (as discusses in Section 3.4). If, in contrast, the transmission coefficient $\mathscr{T}$ was to also effectively depend on the excitation energy of the final state E_f (and thus nuclear temperature T), it would no longer be possible to separate the primary γ-ray matrix $P(E_\mathrm{x}, E_\gamma)$ into two independent functions ρ and $\mathscr{T}$, but we would find

$$P(E_i, E_\gamma) \propto \rho(E_\mathrm{f})\mathscr{T}(E_\mathrm{f}, E_\gamma). \tag{3.41}$$

Simulations were performed with the DICEBOX algorithm [66] on a nucleus that resembles ^{163}Dy to test the effect of a temperature dependent strength function $\gamma\mathrm{SF}(E_\mathrm{f}, E_\gamma)$ with $T \propto \sqrt{E}$. The normal separation procedure was applied to the spectra, where one assumes $P(E_i, E_\gamma) \propto \rho(E_\mathrm{f})\mathscr{T}(E_\gamma)$. For γ energies below about $E_\gamma \approx 2.5\,\mathrm{MeV}$ a strong deviation of the extracted results compared to the (by definition) temperature dependent input is observed. However, the experimental γSFs of several nuclei have been analyzed [69, 72–74], and there is, so far, no evidence of a substantial temperature dependence for excitation energies used here (below about 10 MeV). Thus the Brink-Axel hypothesis is considered to be applicable for the purpose of this work. For further reference, see also a recently published article on the validity of the hypothesis for ^{238}Np [75].

3.8.4. Parity distribution

In the derivation of the level density $\rho(S_n)$ from the neutron resonance spacing D_0, Eq. (3.28), it was assumed that there are equally many positive and negative parity states at the binding energy S_n. In general one would need to multiply Eq. (3.28) by the parity asymmetry parameter α which is defined by the number of positive and negative parity levels $\alpha = (\rho_+ - \rho_-)/(\rho_+ + \rho_-)$. To arrive at an easy form of the normalization of the γSF using the average total radiative width $\langle\Gamma_\gamma\rangle$ in Eq. (3.35) equal parity was even assumed for all excitation energies and spins. Whereas this assumption is questionable for lighter nuclei like iron or molybdenum, it is generally believed to be fulfilled for heavier nuclei and certainly for actinides. For the latter, the level density is so high that one finds a manifold of accessible orbitals even at excitation energies well below S_n. A series of parity distributions which are derived from combinational plus Hartree-Fock-Bogoliubov (HFB) calculations [6] for different nuclei can be found in Ref. [12]. The parity distribution for ^{240}Pu was obtained by the same method and is displayed in Figure 3.9. One observes a well balanced parity distribution from $E_\mathrm{x} \approx 1\,\mathrm{MeV}$.

3.8.5. Spin distribution

The spin distribution is maybe the source of most concern when it comes to the estimation of systematic errors in the Oslo Method. Experimentally it is hardly or not at all accessible for higher excitations energies. Thus there are little constrains for theoretical predictions above about 2-3 MeV . A first impression on different spin distributions can be gained from Figure 3.10, which shows selected predictions for ^{240}Pu with two phenomenological models by von Egidy and Bucurescu of 2005 [58] (hereafter called EB05) and 2009 [76] (hereafter called EB09) and microscopic calculations by Goriely et al. [6]. We now turn our attention to the different ways the spin distribution can influence the results:

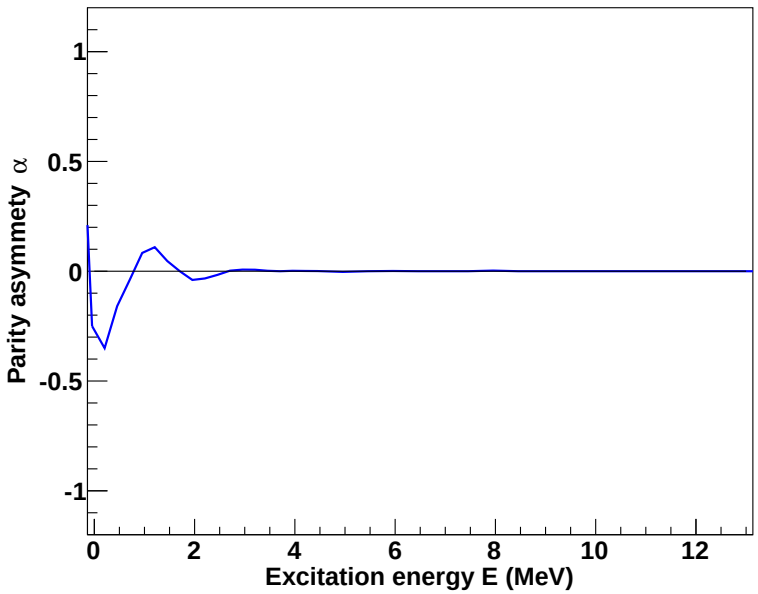

Figure 3.9.: Parity distribution α as a function of excitation energy for ^{240}Pu. Calculated from Ref. [6], data retrieved with RIPL3 [19].

1. Extraction of the first-generations matrix (see Section 3.8.2)
2. Normalization of the level density by $\rho(S_n)$
3. Normalization of the γ-ray strength function
4. Mismatch of the experimentally populated spins (typically 0 to 8 $\hbar$, depends on target spin and reaction) and the total spin range

As mentioned in Section 3.6, previous analyses in the actinide region [14, 16] suggest that the light ion (d, p) reaction used in this experiment may not transfer enough spin to populate the total spin range of the target nucleus. Currently, we have no prediction on the experimentally populated spins. In the standard procedure for the Oslo Method, the levels which were not populated are assumed to contribute on average with a scaling dependent on a factor r, see Eq. (3.34). This factor is automatically corrected for when the total level density is obtained by the usual normalization to $\rho(S_n)$. This implies the assumption, that the structure of the level density is not strongly affected, e.g. due to nucleon pair breaking.

The sensitivity of the Oslo Method on the experimentally accessed spin window has partially been tested with the COMBI code [74, 77]. It calculates the level density of a nucleus based on a microscopic, combinatorial model using Bardeen-Cooper-Schrieffer (BCS) quasi-particles and the Nilson single-particle level scheme.

The resulting level densities only using levels with spins (i) $0 \leqslant J \leqslant 6$ and (ii) $0 \leqslant J \leqslant 30$ are displayed for ^{56}Fe and ^{164}Dy in Figure 3.11 together with the experimental data extracted with the Oslo method, Ref. [78] and Ref. [72] respectively. In both nuclei the general structure of the level density is very similar for the different spin ranges. For ^{56}Fe, the difference between results for the small and large spin window are at maximum 30%. Here no severe problems

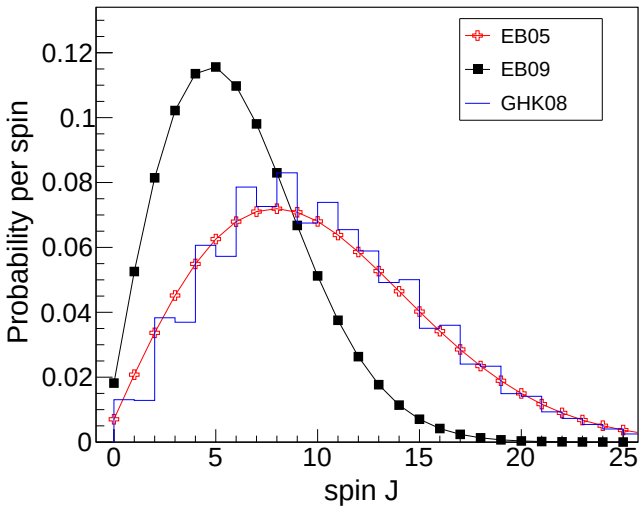

Figure 3.10.: Spin distributions of ^{240}Pu at an excitation energy of $E_x = S_n$. The microscopic calculations of Goriely et al. [6] (blue) agree well with the phenomenological approach of von Egidy and Bucurescu [58] of 2005 (red). Also shown is their latest model [76] of 2009 (black).

are expected in the normalization of the level density to the value at the binding energy $\rho(S_n)$ (and subsequent normalization of the γSF with this density). However, for the heavier nucleus ^{164}Dy, the two cases deviate by a factor of about 2.5 at $E \approx 7.5$ MeV. As ^{240}Pu is even heavier than ^{164}Dy, it has a higher total level density, so the effect is potentially even stronger here. For a proper normalization of the γSF with the average total radiative width $\langle\Gamma_\gamma\rangle$ following Eq. (3.35), one would need a better estimation of the reduced level density ρ_{red}. In lack of that, we have to work with extrapolations of photo-nuclear data, as is described in Section 3.6.

For the upper normalization point of the level density we calculate the number of levels at the neutron separation energy $\rho(S_n)$ as a function of the neutron resonance spacing for s-waves D_0. Any equation that relates these two quantities is inevitably linked to the spin distribution; the derivation of Eq. (3.28) assumed the model of Gilbert and Cameron [57]. To test the dependence of the final results on the distribution of initial spins, three scenarios were simulated with the DICEBOX code [66] for two different (artificial) nuclei. The first relatively light nucleus resembles ^{57}Fe and the second, heavier nucleus resembles ^{163}Dy.

Three spin ranges were simulated: (i) $1/2 \leqslant J \leqslant 7/2$, (ii) $1/2 \leqslant J \leqslant 13/2$, and (iii) $7/2 \leqslant J \leqslant 13/2$ where the weighting followed the spin distribution of the input level density, in this case microscopic calculations of Ref. [6]. For each initial spin range the full Oslo method was applied to gain the level density and γ-ray strength function. Figure 3.12 shows the results for the light nucleus.

Whereas a strong enhancement of the extracted γ-ray strength function at low energies is observed for the light nucleus in cases (ii) and (iii), no such deviation was seen for the heavier nucleus. By a simultaneous analysis of the true first-generations matrix (which is part of the DICEBOX [66] generated data), it was also checked that the deviation is not simply an anomaly introduced by the unfolding or first-generations method. The finding is attributed to

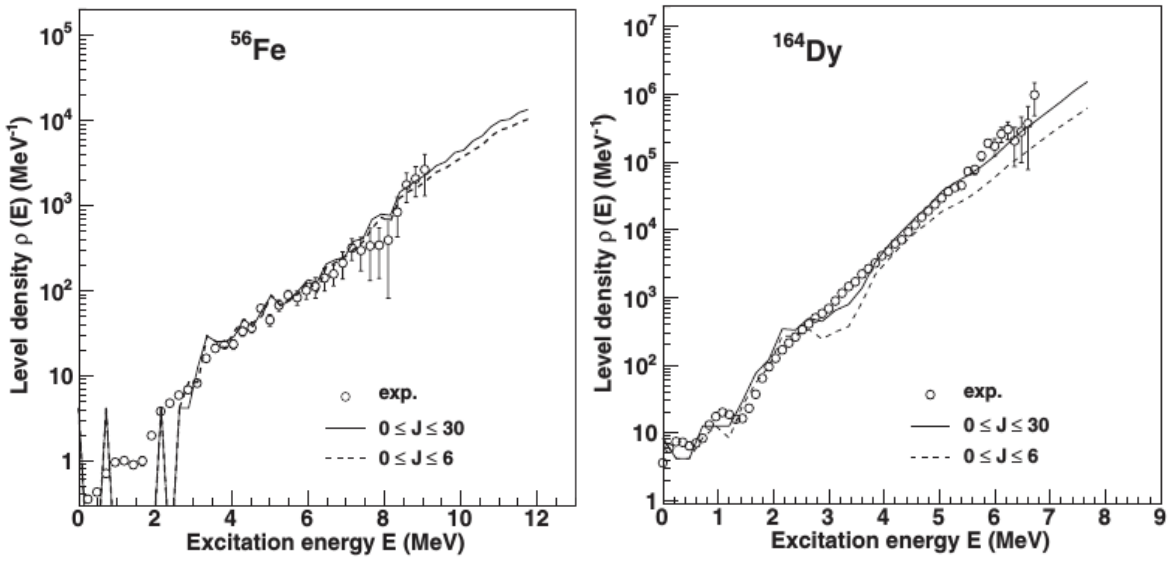

(a) (b)

Figure 3.11.: Level densities for (a) ^{56}Fe and (b) ^{164}Dy, calculated with COMBI for two spin ranges: (i) $0 \leqslant J \leqslant 6$ (dashed line) and (ii) $0 \leqslant J \leqslant 30$ (solid line). For comparison we also show the experimental data (open circles), Ref. [78] and Ref. [72] respectively, which are normalized to the total level density at S_n. Reproduced from [12].

the fact that for lower mass nuclei the high spin levels are missing at low excitation energies. Taking into account the restricted initial spin range, this implies that a higher spin level (e.g. $J = 13/2$) at high excitation energy can not directly decay to low energies by dipole radiation. The only way to get to lower excitation energies with dipole transitions is through a cascade, thus increasing the probability to decay with several low-energy γ-rays. For higher mass nuclei the level density is so high, that even at low excitation energies relatively high spin states are accessible. Thus the normalization procedure for low mass nuclei is more susceptible to differences in the spin distribution. An enhancement of the γSF at low excitation by the procedure itself is consequently not expected for ^{240}Pu.

3.8.6. Impact on this work

Summing up the different aspects mentioned in this section, the spin distribution is considered to be the element potentially introducing the highest error to our calculations. The level density $\rho(S_n)$ deduced from D_0 with the spin distribution of Gilbert and Cameron [57] is (i) $32.7(66) \times 10^6\,\mathrm{MeV}^{-1}$ with the spin cut-off parameter σ of EB05 [58] and (ii) $12.9(25) \times 10^6\,\mathrm{MeV}^{-1}$ with σ of EB09 [76]. In Figure 3.10 we can observe that the distribution extracted with option (i) is very similar to results from microscopic calculations by Goriely et al. [6], thus in principal we recommend this option. However, lacking experimental information about the true distributions, we decided to pursue the analysis again for two more scenarios and use these to span an error band for our results.

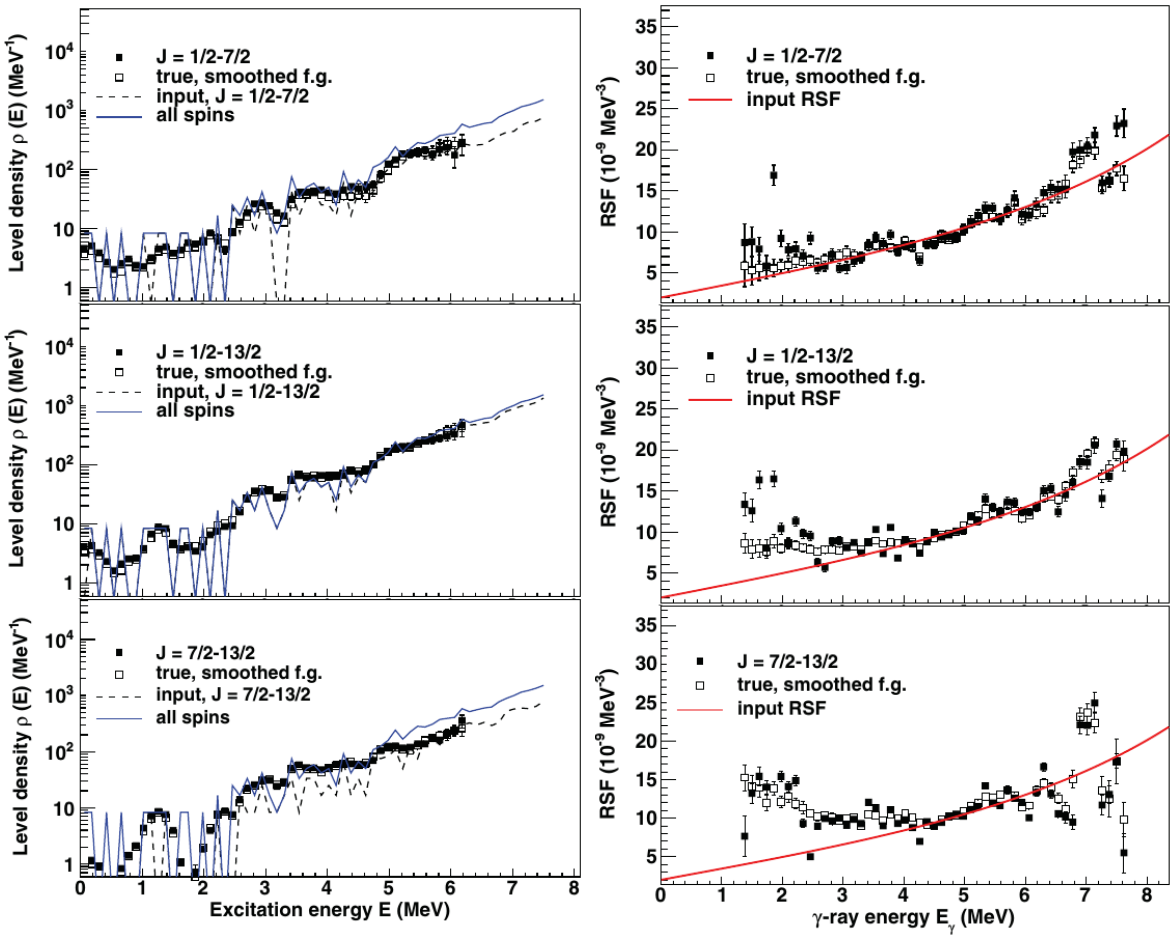

(a) (b)

Figure 3.12.: Extracted level densities (a) and γSF (b) from DICEBOX [66] calculations on a nucleus resembling ^{57}Fe for spin range $1/2 \leqslant J \leqslant 7/2$ (top),$1/2 \leqslant J \leqslant 13/2$ (middle) and $7/2 \leqslant J \leqslant 13/2$ (bottom). For comparison also the results extracted from the true (DICEBOX generated) first-generations matrix and the input functions are shown. Reproduced from [12].

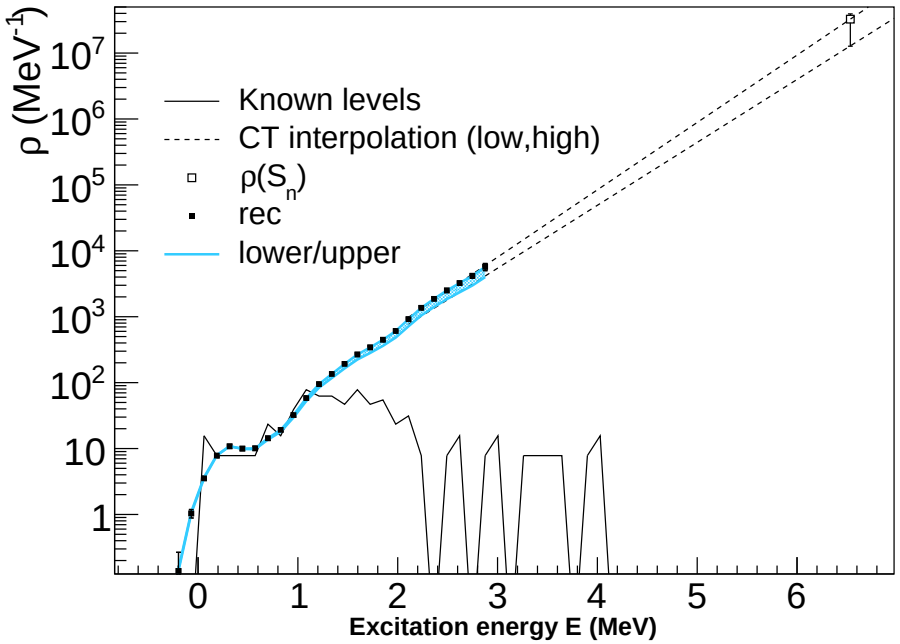

Figure 3.13.: Level density obtained with the Oslo method. The back points show the normalization with the spin cut-off parameter σ from EB05 [58], which is simultaneously the upper limit of the error band (azure line). The lower limit is given by results using the spin cut-off parameter from EB09 [76].

For the total level density of the nucleus we assume that the (potentially) not populated levels in the experiment due to spin restrictions are compensated for by the normalization to $\rho(S_n)$. Thus the recommended values are those extracted in Section 3.5, which is equivalent to first option above. The lower limit for the error band is formed by the second option; all values used in the extraction are listed in Table 3.4. The results are displayed in Figure 3.13.

The extraction of the γ-ray strength function also depends on the level density and thus the spin distribution models. The recommended values are those obtained in Section 3.6, where we used option (i) but reduced the level density $\rho_{\mathrm{red}} = 18 \times 10^6\,\mathrm{MeV}^{-1}$ to account for the experimentally populated spin range. As the extend to which the reduction is necessary is relatively uncertain, we form the error band by taking the total level density instead and once again we use both options above for the spin cut-off. The γ-ray strength function including the error band is shown in Figure 3.14.

Finally, a change in the γ-ray strength function in general has an impact on the extracted the scissors resonance. The shape and strength was reanalyzed with the same procedure as in Section 3.7, including a re-fitting of the assumed background for each case. In Figure 3.15 it can be observed that the general shape of the scissors resonance is preserved. The results for the strength and energy centroid are listed in Table 3.4.

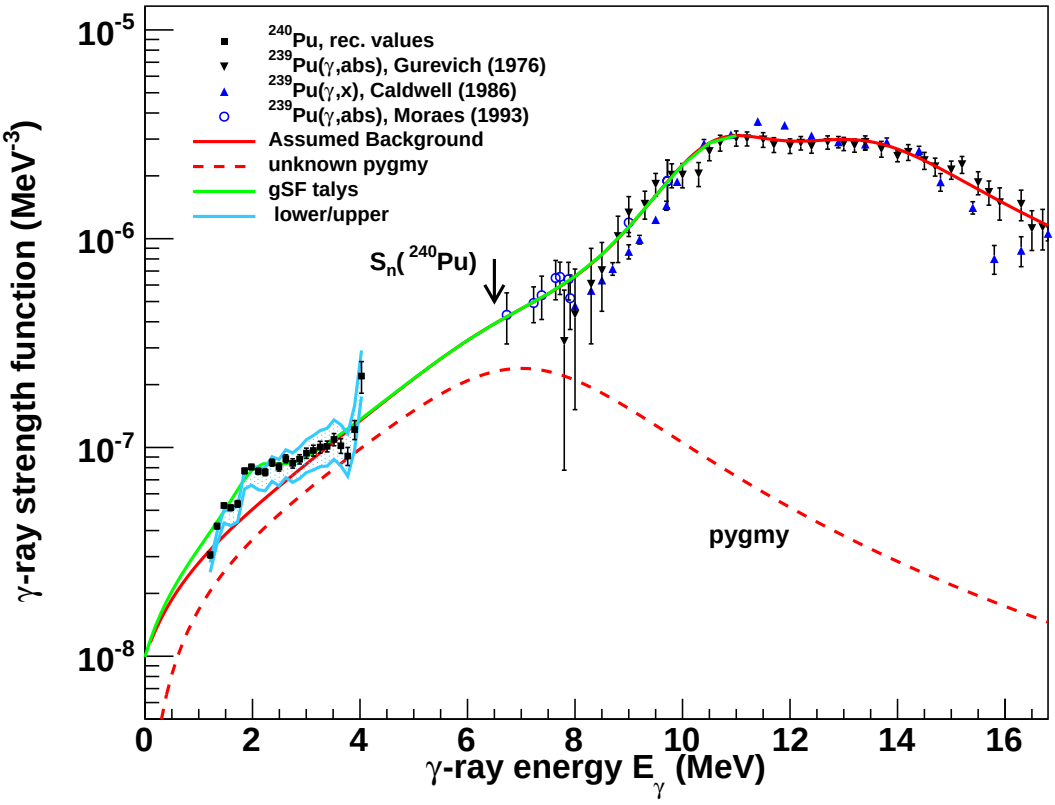

Figure 3.14.: γ-ray strength function obtained with the Oslo method. The back points show the normalization with the spin cut-off parameter σ from EB05 [58], but extracted with a reduced level density $\rho_{\mathrm{red}} = 18\times10^{6}\,\mathrm{MeV}^{-1}$. The upper limit of the error band (azure line) is determined using the total level density. The lower limit is given by applying the spin cut-off from EB09 [76]. The solid red line represents the estimated strength without the scissors resonance, deduced from extrapolation of photo-absorption data by Gurevich et al. [61], Caldwell et al. [62] and De Moraes and Cesar [63].

Table 3.4.: Parameters used to extract level density and γ-strength function for the different spin cut-offs by Ref. [58, 76]. Where applicable, references are stated next to the variable. For all cases we used $S_n = 6.53420(23)$ MeV [46], $D_0 = 2.20(9)$ eV [19] and $\langle\Gamma_\gamma(S_n)\rangle = 43(4)$ MeV [19].

Case	a [58] [MeV^{-1}]	E_1 [58] [MeV]	$\sigma(S_n)$	T_{CT} [MeV]	$\rho(S_n)$ [10^6 MeV^{-1}]	$\rho(S_n)_{\mathrm{red}}$ [10^6 MeV^{-1}]
EB05 & ρ_{red}	25.16(20)	0.12(8)	8.43(80)	0.425(1)	32.7(66)	18
EB05 & ρ_{tot}	25.16(20)	0.12(8)	8.43(80)	0.425(1)	32.7(66)	–
EB09 & ρ_{tot}	23.08(16)	0.33(6)	5.23(50)	0.455(1)	12.9(25)	–

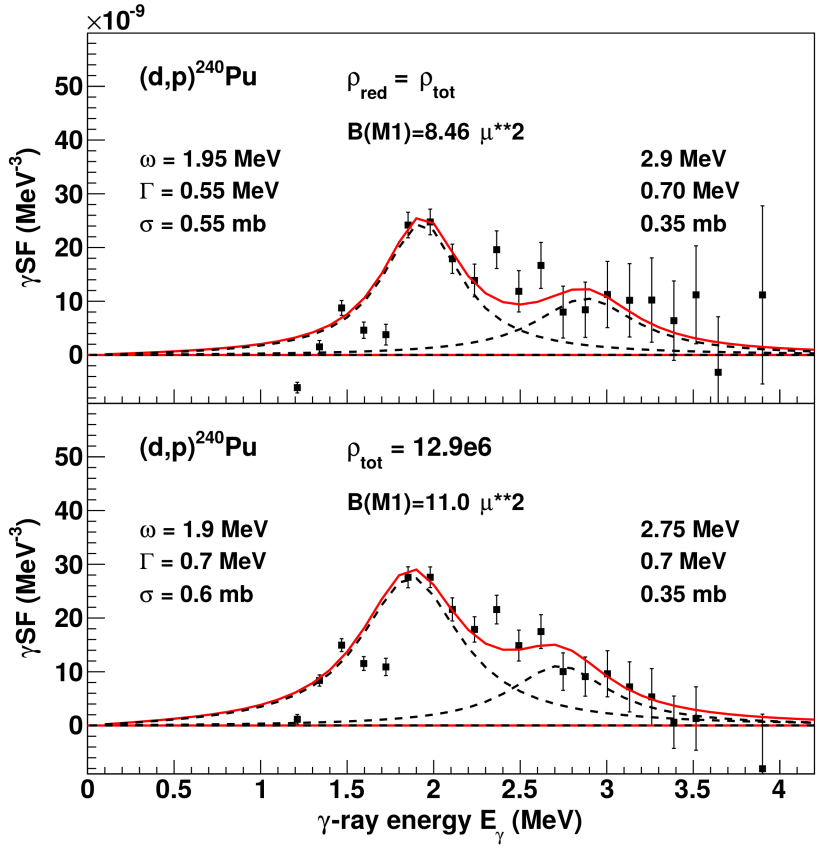

Figure 3.15.: The extracted scissors resonances using the total level densities and the spin cut-off of EB05 [58] (top) and EB09 [76] (bottom) including a re-fitting of the base-line. They are fitted with two SLO resonances (dashed lines) and the parameters are given in the plots. The drop in the data points between 1.6 to 1.9 MeV is assumed to be linked to a very strong peak in the coincidence-matrix, that could not be sufficiently accounted for in the primary γ-ray extraction procedure.

Table 3.5.: Parameters of the scissors resonance extracted with spin cut-off parameters taken from EB05 [58] and EB09 [76]. For a comparison, the top row shows the estimate using a reduced density ρ_{red}. The sum rule estimates are $\omega_{\mathrm{SR}} = 2.24\,\mathrm{MeV}$ and $B_{\mathrm{SR}} = 10.1\mu_{\mathrm{N}}^2$.

Case	Lower resonance				Upper resonance				Total	
	$\omega_{\mathrm{SR},1}$ [MeV]	$\sigma_{\mathrm{SR},1}$ [mb]	$\Gamma_{\mathrm{SR},1}$ [MeV]	$B_{\mathrm{SR},1}$ [μ_{N}^2]	$\omega_{\mathrm{SR},2}$ [MeV]	$\sigma_{\mathrm{SR},2}$ [mb]	$\Gamma_{\mathrm{SR},2}$ [MeV]	$B_{\mathrm{SR},1}$ [μ_{N}^2]	ω_{SR} [MeV]	B_{SR} [μ_{N}^2]
EB05 & ρ_{red}	1.90(05)	0.68(5)	0.60(10)	7.6(14)	2.70(10)	0.35(5)	0.75(15)	3.4(9)	2.15(6)	11.0(16)
EB05 & ρ_{tot}	1.95(05)	0.55(5)	0.55(10)	5.5(12)	2.90(10)	0.35(5)	0.70(10)	3.0(6)	2.28(7)	8.5(13)
EB09 & ρ_{tot}	1.90(05)	0.60(5)	0.70(10)	7.8(13)	2.75(15)	0.35(5)	0.70(10)	3.1(7)	2.14(6)	11.0(15)

3.9. Cross-section calculations

Level densities and γSFs are essential inputs to cross-section calculations for nuclear reactions in a statistical framework. We have performed calculation with the reactions code TALYS v1.6 [25] which produces (n, γ) cross-sections based on our data and a neutron optical model potential (nOMP).

In order to use the level density and γSF extracted in this work, the databases and source code of TALYS have to be modified slightly. We altered the level density model to include the discrete level scheme up to 1.09 MeV and afterwards follow a constant temperature formula. The source code of the strength function was adopted to an EGLO for the GEDR which was used in the current analysis. It can be seen in Figures 3.14 and 3.16 that the implemented level density and strength function then closely follow our results.

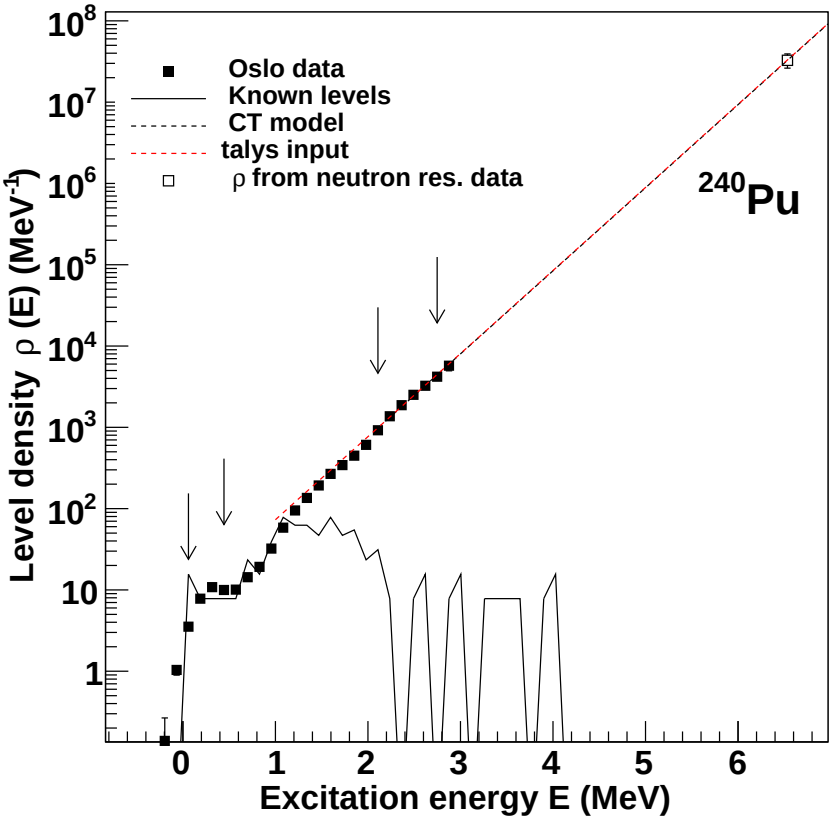

Figure 3.16.: Level density obtained with the Oslo method compared to the input for TALYS calculations. Up to 1.09 MeV TALYS uses the discrete level scheme.

We performed calculations with both neutron optical model potentials available for actinides in TALYS v1.6. According to the manual, the default option for actinides apparently implements the nOMP of Soukhovitskii et al. [79], although it is only invoked by the keyword *localomp n*. The potential itself is in very good agreement with experimental data. However,

Table 3.6.: The predicted average resonance parameters from the present analysis, from Soukhovitskii et al. [79], and data extracted from experiments by Mughabghab and Dunford [81]. For comparison also calculations for ^{238}U are shown.

Model		^{238}U			^{239}Pu		
		S_0 [10^{-4}]	S_1 [10^{-4}]	R [fm]	S_0 [10^{-4}]	S_1 [10^{-4}]	R [fm]
TALYS v1.6[12]	Koning LocalOMP	0.38	2.32	8.95	0.44	0.47	9.15
	"Soukhovitskii" OMP	0.63	1.50	9.49	0.62	0.68	9.45
Reference Values	Soukhovitskii[13][79]	0.95	1.80	9.57	0.93	1.77	9.56
	Mughabghab [81]	1.2(1)	1.7(3)	9.6(1)	1.3(1)	2.3(4)	9.6(3)

a detailed study of the TALYS output shows that important bench-mark parameters from the implemented potential [79] are not reproduced. A comparison between different results for the average resonance parameters, the neutron strength functions S_0 and S_1 and the potential scattering radius R, is displayed in Table 3.6. Although considerable effort has been spend to trace back the origin of the discrepancy, we were not yet able to rectify the issue. The second available option is an optical model potential by Koning and Delaroche [80]. This is a local model but not optimized for the actinide region and thus quite naturally does not reproduce the experimental average resonance parameters of ^{239}Pu either. Due to these discrepancies, it is difficult to asses the reliability of the calculated cross-sections. The results presented in the following are therefore considered preliminary.

The calculated cross-sections are displayed in Figure 3.17, together with experimental data by Hopkins and Diven [82], Kononov et al. [83] and Schomberg et al. [84]. It can be observed that the choice of different optical model potentials has a strong impact on the cross-section calculations. The calculations with both OMP options fail to reproduce the experimental data. Whilst this could hint at an erroneous level density and γ-ray strength function, only very small differences were seen when using the results obtained from different spin cut-off parameters in the previous section as input to the calculations. Thus the discrepancy is considered more likely to be an effect of the implemented OMPs failure to reproduce the experimental average resonance parameters.

[13]Note that there is a slight energy dependence on these values. The displayed results are extracted for $E = 3.25 \times 10^{-5}$ eV.

[13]Soukhovitskii et al. [79] gives the neutron strength functions S_0 and S_1 in units of $(\text{eV})^{-1/2} \times 10^{-4}$. The values have been adopted to the standard dimensionless quantity [19, 81], which is justified by a comparison of values referred to within his work.

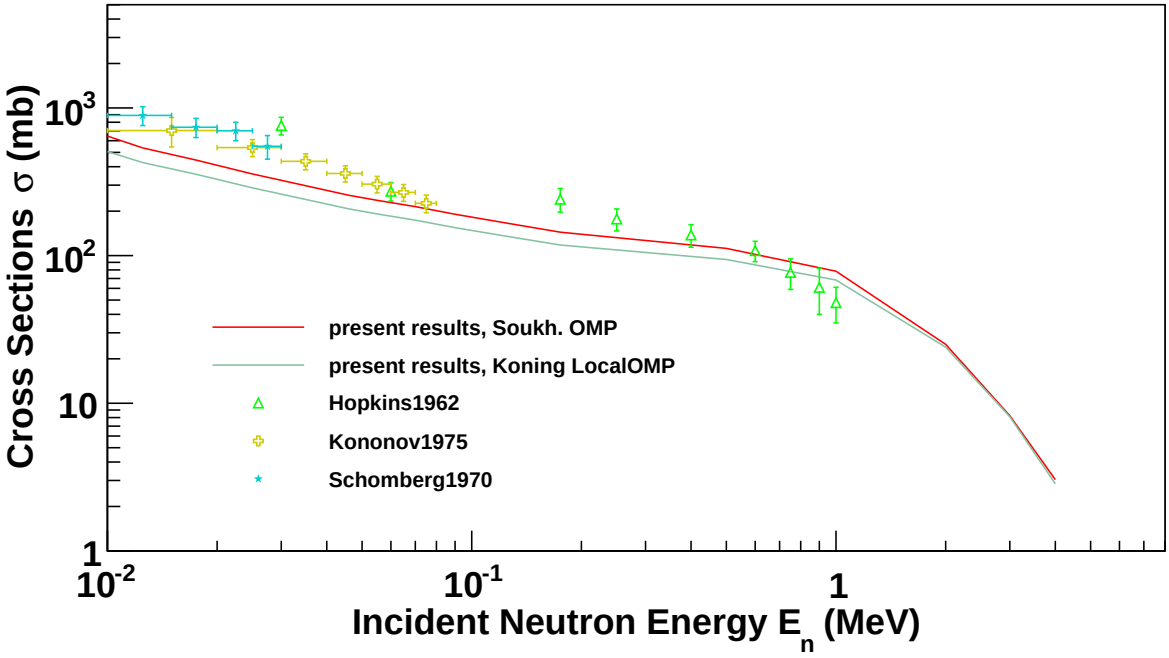

Figure 3.17.: Preliminary ^{239}Pu(n, γ) cross-sections calculated with TALYS v1.6 using level density and γ-ray strength obtained in this work. For comparison experimental data by Ref. [82–84] are displayed (see legend). Both optical model potentials in their current implementation do not reproduce average resonance parameters and thus the calculated cross-sections do not match experimental data.

Chapter 4.
4 Discussion

In the previous chapter we extracted the level density and γ-ray strength function for ^{240}Pu. Moreover, we established the presence of an enhanced strength between 1 and 4 MeV that is interpreted as the M1 scissors resonance. Finally, the neutron capture cross-section for $^{239}\mathrm{Pu}(\mathrm{n},\gamma)$ was calculated. In the following we compare these results to other analyses in the actinides region and stress the implications for selected application. Particular attention will be given to similarities and differences to recent results for ^{243}Pu [17].

Historically, the first theoretical attempt to describe nuclear level densities was undertaken by Bethe [18]. In his work, he described the nucleus as a gas of noninteracting fermions with equally spaced single-particle levels. This model was later adopted to include an excitation energy shift parameter E_1 due to pairing correlations between nuclei. It has been widely used and the popularity can be seen, for example, by its listing in the nuclear data library RIPL3 [19].

The main feature of the (back-shifted) Fermi-gas model is that the nuclear temperature is connected to the excitation energy by $T \propto \sqrt{E}$. However, recent publications in the quasi-continuum region show more support for a constant temperature dependence of the level density above $E = 2\Delta$, where Δ is the pairing gap parameter. This is derived both from particle evaporation techniques [85] and the Oslo Method. The new result is rather surprising, as there is currently no fundamental theoretical explanation for such a behavior.

A constant temperature dependence of the level density could be expected if the whole nucleus was in contact with one large heat bath [13]. However, there is no source for a heat bath in an isolated system like the nucleus. Moreover, in Ref. [86] level densities have been calculated for canonical, grand canonical and microcanonical ensembles, all of them yielding a Fermi-gas like temperature dependence. A first explanation has been proposed by Guttormsen et al. [13] arguing that a continuous melting of Cooper pair is the source of the constant temperature dependence. To develop and test a new theory that could explain this behavior, the accessibility of experimental data is highly important. In recent years there has been an increasing effort to study properties of nuclei in the actinide region. The publications include observations for $^{231-233}$Th, $^{232-233}$Pa, $^{237-239}$U [13–15], ^{238}Np [16] and ^{243}Pu [17]. In Figure 4.1 the extracted level densities for ^{240}Pu are shown together with data for ^{243}Pu [17] and for the uranium isotopes [13]. All of them are in good agreement with the constant temperature formula which is used to interpolate the results to $\rho(S_n)$. The limited excitation energy range usable for ^{240}Pu does not allow a conclusive decision on either the constant temperature or Fermi-gas model for this nucleus. However, we assume that there is no reason to expect that ^{240}Pu should behave very differently than other nuclei in the region.

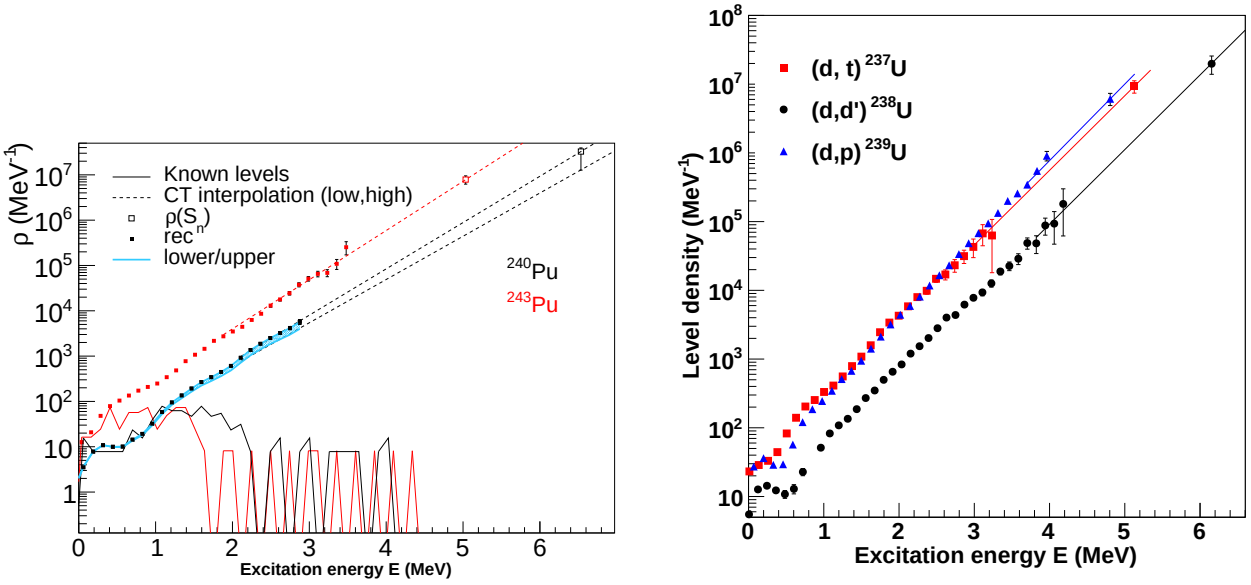

(a) (b)

Figure 4.1.: Level density obtained with the Oslo method for (a) ^{240}Pu (black) and ^{243}Pu [17] (red) and (b) $^{237-239}$U [13] (see legend). For ^{240}Pu an error band is given resulting from different spin cut-off parameters. The level densities follow a constant temperature formula (interpolation lines). Note that the discrete levels for normalization are only shown for the plutonium isotopes. Figure (b) is reproduced from Ref. [13].

In a similar manner, the theory of the γ-ray strength function has been subject to large modifications. The first experiments using (γ, n) reactions revealed a strong, resonance-like structure called the Giant Electric Dipole Resonance (GEDR) at excitation energies of approximately 10-14 MeV [20]. This was explained in a macroscopic picture, with protons oscillating against neutrons. As common for resonating systems, a Lorentzian shape was assumed. With the discovery of several resonances on top of the low energy tail of the GEDR the picture has become more complex. The possibility to study the strength function below the neutron separation threshold enabled the Oslo nuclear physics group to discover an energy enhancement below 2-3 MeV for many nuclei [73, 87] that is now known as the upbend. Moreover, for the energy range between 1-4 MeV several nuclei exhibit an excess strength that is identified as the scissors resonance.

In Figure 4.2 the γ-ray strength function found in the current analysis is displayed together with previous results extracted with the Oslo Method in the actinide region. The experimental data above the neutron separation energy used in the normalization is taken from Gurevich et al. [61], Caldwell et al. [62], De Moraes and Cesar [63] for ^{240,243}Pu and the works stated within Ref. [14, 16] for all other nuclei. Obviously all data sets exhibit an additional strength between 1 and 4 MeV that fits with the energy region predicted for the scissors mode. Additionally, the results for ^{238}Np and ^{243}Pu postulate not only a pygmy resonance at around 7 MeV necessary to fit the (γ, x) results, but also a second pygmy resonance at 5.5 and 4.4 MeV, respectively.

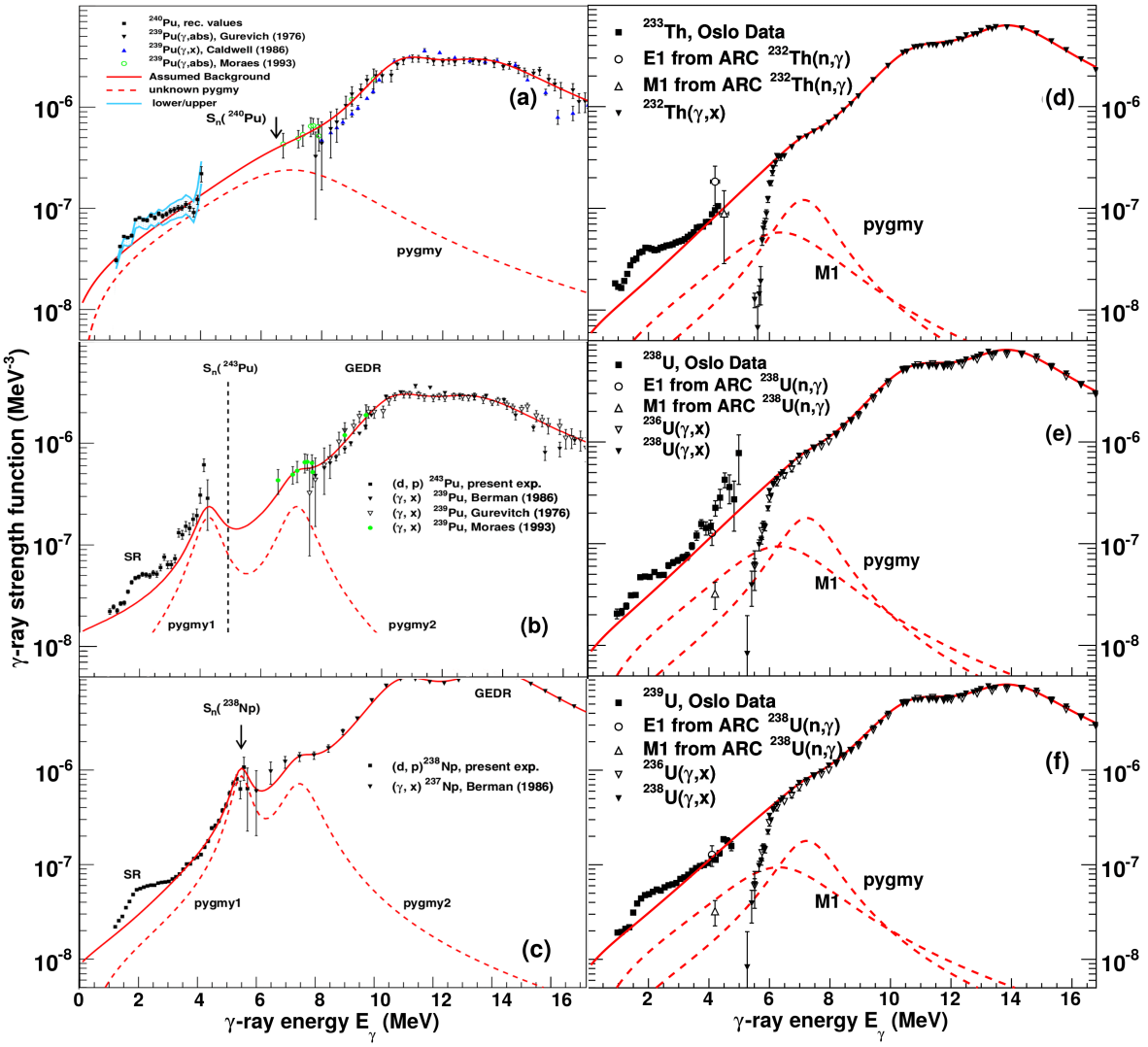

Figure 4.2.: The γ-ray strength function obtained with the Oslo method for different nuclei. The panels show the present results for ^{240}Pu including the error band (a), compared to ^{243}Pu [17] (b), ^{238}Np [16] (c), ^{233}Th [14] (d), ^{238,239}U [14] (e,f). For the reference to the experimental (γ, x) data used in the normalization, see reference within these works. All γSFs exhibit an excess strength between 1-4 MeV that is interpreted as the scissors mode.

The current dataset may hint to a similar second resonance at around $\approx$ 5 MeV; however to reach this γ-ray energies in ^{240}Pu, it would be necessary to extract data above the onset of fission events and pile-up. This has been preformed for demonstration purposes and is displayed Figure 4.3, but due to the mentioned constrains for ^{240}Pu we do not think that those findings would be very reliable. On the contrary, the rigorous analysis conducted in Section 3.6 does not require a second resonance. In order to minimize the number of assumptions introduced, we therefore postulate only one additional resonance at 7.5 MeV.

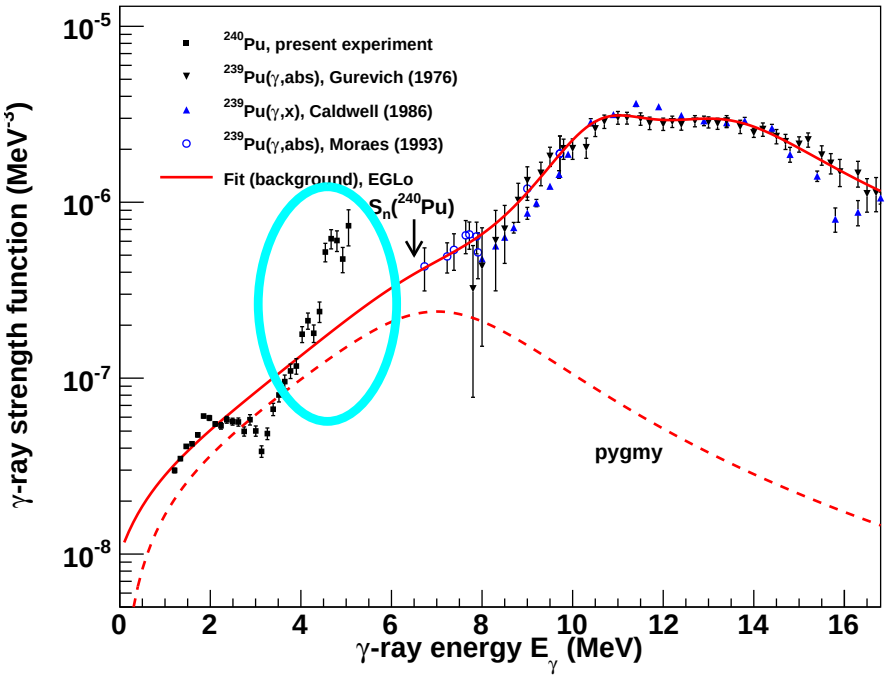

Figure 4.3.: The γ-ray strength function obtained with the Oslo method for ^{240}Pu when extracting data up to $E_x = 5.1\,\mathrm{MeV}$. This dataset may hint at an additional resonance around 5 MeV (highlighted), however to reach so high γ-ray energies in ^{240}Pu, it is necessary to extract data above the onset of fission events and pile-up at $\approx$ 4MeV. This extended data is not considered very reliable. For the results proposed in this work, see e.g. Figure 4.2 (a).

For all nuclei the scissors mode was extracted and is shown in Figure 4.4. A common feature is the double humped structure of the resonance. The current experiment yields an average centroid $\omega_{\mathrm{SR}} = 2.15(6)\,\mathrm{MeV}$ and a summed $B(M1)$ strength of $B(M1) = 11.0(16)\,\mu_{\mathrm{N}}^2$. The systematic errors of different spin distributions are approximately of the same order then the statistical uncertainties[1]. This is in good agreement with previous experiments from the Oslo group for the above named nuclei, which result in an average centroid $\langle\omega_{\mathrm{SR}}\rangle = 2.38(16)\,\mathrm{MeV}$ and the average summed $\langle B(M1)\rangle$ strength of $\langle B(M1)\rangle = 9.2(16)\,\mu_{\mathrm{N}}^2$.

Experiments conducted by several other groups have determined the scissors states build on the ground state by (γ,γ') and (e,e') reactions [21–23]. Typically they yield $B(M1)$ strength between 2-4 μ_{N}^2 in the actinide region. This is about a factor of 2-3 lower than the results in of the Oslo group. There is at least two explanations that may resolve these discrepancies.

First, the $B(M1)$ strength of the scissors mode is proportional to the moment of inertia $B(M1) \propto \Theta$. With the Oslo method one observes the scissors resonance in the quasi continuum, where a rigid-body momentum of inertia Θ_{rigid} is assumed. For resonances build on the ground-state naturally the ground-state moment of inertia Θ_{gs} is used. For even-even nuclei in the actinide region the ratio between these values is $\Theta_{\mathrm{ridig}}/\Theta_{\mathrm{gs}} \approx 2$. For ^{232}Th results are available

[1]Note that the uncertainty in the estimation of the GDR tail is not included.

from both the Oslo Method and HIγS and there is a good agreement with the aforementioned hypothesis: $\sum B(M1)_{\text{Oslo}} / \sum B(M1)_{\text{HI}\gamma\text{S}} = 2.2(7)$ [14].

Another reason why typically less strength is found by analysis of HIγS data could be that it relies on identification of single states in a region where the level density reaches 10^3-10^5 MeV^{-1} [14]. Thus potentially not all strength is resolved experimentally. In this light it is interesting that a recent measurement of discrete states at HIγS has discovered a $B(M1)$ strength of $8.1(1)\mu_{\text{N}}^2$ for ^{238}U, where two-thirds of it being attributed to the scissors mode [88]; this is higher then typical for HIγS.

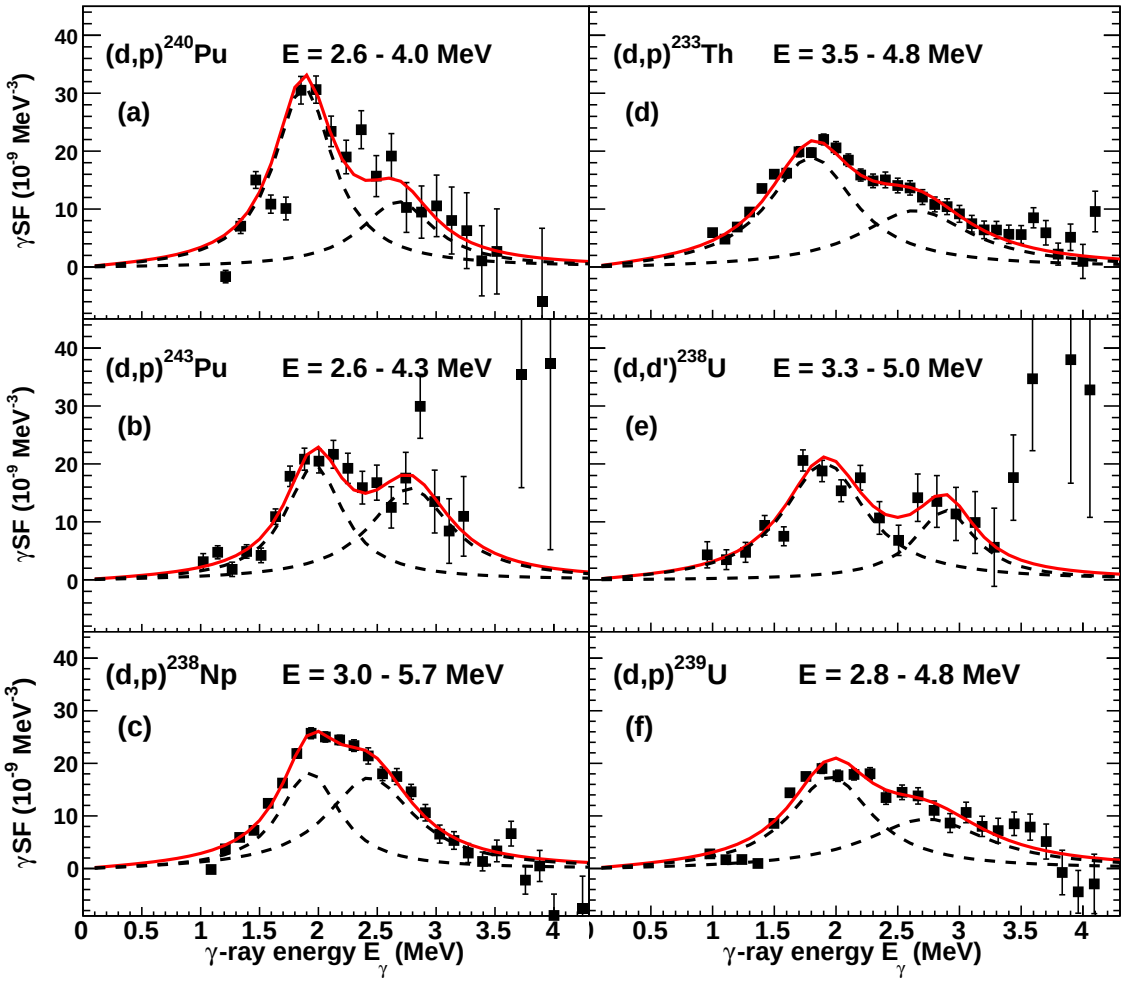

Figure 4.4.: Scissors resonance obtained with the Oslo method for different nuclei. The panels show the present results for ^{240}Pu (a), compared to ^{243}Pu [17] (b), ^{238}Np [16] (c), ^{233}Th [14] (d), ^{238,239}U [14] (e,f). Also given is the excitation energy range used in the analysis.

We have attempted to explore the impact of the current results on the $^{239}\text{Pu}(\text{n},\gamma)$ cross-section through calculations with the TALYS [25] nuclear reactions code. From the level density and γ-ray strength function extracted in this work and a suitable neutron optical model potential the cross-sections can be calculated. However, as discusses in the previous section,

the best available potential by Soukhovitskii et al. [79] seems to be erroneously implemented as neither results from the original paper, nor experimental average neutron resonance parameters could be reproduced. The cross-sections calculated with this potential are displayed in Figure 4.5. However, they are considered highly preliminary, and emphasize the need to solve the problems in the implementation of the potential. As a comparison, the results from other experiments [82–84] and the nuclear data libraries ENDFB/VII.1 [26] and JENDL-4.0 [27] are shown.

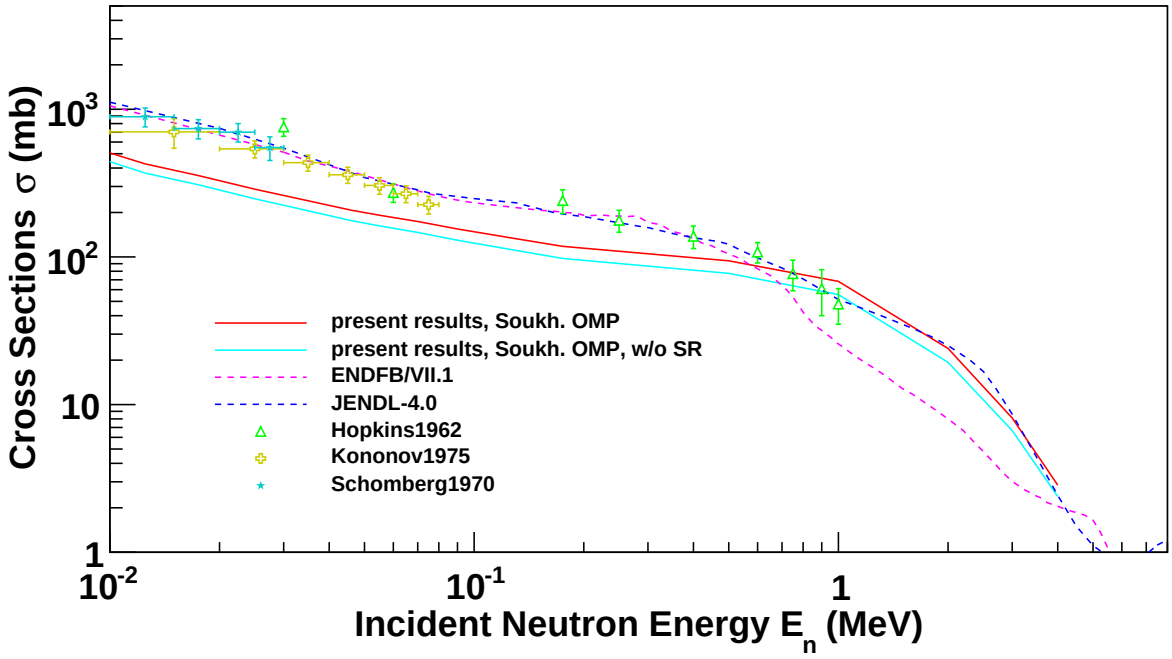

Figure 4.5.: Preliminary ^{239}Pu(n, γ) cross-sections calculated with TALYS v1.6 using level density and γ-ray strength obtained in this work with the OMP of Ref. [79]. There is a 25 % increase of the cross-section when the scissors resonance is included (red line). For comparison experimental data by Ref. [82–84] and the nuclear data libraries ENDFB/VII.1 [26] and JENDL-4.0 [27] are displayed (see legend). There is a large discrepancy between the two libraries for incident neutron energies above about 0.5 MeV.

Accurate knowledge of neutron capture cross-sections is essential for advanced reactor systems. Recent studies by the OECD Nuclear Energy Agency (NEA) analyzed the data needs for such systems [28, 29]. With six fast neutron reactors out of the eight systems under consideration, there are tight requirements on target accuracies (usually well below 10 %) for actinide neutron capture cross-sections at energies between several keV and MeV. Therefore one should note the large differences between the nuclear data libraries for incident neutron energies E_n above around 0.5 MeV. At maximum, the cross-sections given by JENDL-4.0 [27] are up to about half an order of magnitude larger than for ENDFB/VII.1 [26]. The reference

paper to ENDFB/VII.1 states that "[i]n the keV - MeV range, radiative neutron capture cross sections for ^{235}U and ^{239}Pu are poorly known: the covariance evaluation in ENDF/B-VII.1 has capture uncertainties of the order of 15% for each of these nuclei. These reactions are so important that should new assessments, based on new measured data, lead to significant changes in these evaluated cross sections, there will be significant implications for nuclear applications, for example in our criticality calculations." [26] With a more reliable implementation of the OMP, it can be assumed that our results will confine the resulting uncertainty considerably.

Moreover, the determination of the neutron capture cross-sections is of importance in astrophysical applications like the estimation of the actinide abundance, as rapid neutron capture is the only process that can lead to the formation of actinide nuclei [30]. Given the abundances and cross-sections for these nuclei, one can for example estimate the age of the universe. Our results may have a direct impact by narrowing down the uncertainty for the neutron capture cross-section of ^{239}Pu.

Even more important might be an indirect contribution. The nucleosynthesis of heavy elements involves the reaction rates of exotic nuclei which are far from the stability line and thus unaccessible to direct measurements of cross-sections. With the described method, capture cross-sections for these nuclei can be calculated. However, their accuracy crucially depends on the input models. To the authors knowledge, the scissors resonance has up to now not been included in such calculations. Although there might be a discussion about the exact strength of the scissors mode, with the increasing number of experiments that have been conducted, it can certainly be assumed that the resonance is a general feature of the actinides region - and possibly even beyond. In Figure 4.5 it can be observed, that the inclusion of the scissors resonance changes the cross section for $^{239}\mathrm{Pu}(\mathrm{n},\gamma)$ by about 25%. Similar deviations have been found for other actinides, where cross-section calculations have been obtained from the Oslo data [16, 17]. Note that we have not renormalized the γ-ray strength function without the scissors resonance to the average radiative width $\langle\Gamma_\gamma\rangle$. This reflects the situation for the large number of nuclei where no data on $\langle\Gamma_\gamma\rangle$ exists. In the light of these findings we see a strong need to include the scissors resonance in model calculations of the r-process and study the impact on the resulting abundances and estimations of the age of the universe.

5 Chapter 5. Conclusions and outlook

"Go back?" he thought. "No good at all!
Go sideways? Impossible! Go forward?
Only thing to do! On we go!"

J.R.R. Tolkien
The Hobbit

This thesis was motivated by the search for more detailed descriptions of the level density and γ-ray strength function of ^{240}Pu below the neutron separation energy. These are also the main input for calculations of the neutron capture cross section of ^{239}Pu which is of significance for applications in reactor and astrophysics.

A ^{239}Pu target was bombarded with 12 MeV deuterons at the Oslo Cyclotron Laboratory (OCL). The particle-γ coincidences from the (d, p) reaction have been selected and converted to the γ-ray spectrum emitted at each excitation energy.

A set of techniques collectively known as the Oslo method have been applied to this data in order to extract the level density and γ-ray strength function of ^{240}Pu in the quasi-continuum. In order to remain selective on deexcitation by γ-rays, only data for excitation energies below the neutron separation energy at about 6.5 MeV have been analyzed. A further constrain was given by sub-barrier fission resonances that were observed at approximately 5 MeV, which is 1 MeV below the fission barrier of ^{240}Pu.

Previous studies on $^{231-233}$Th, $^{232-233}$Pa, $^{237-239}$U [13, 15] revealed a constant temperature behavior of the level density. This is a surprising finding as it stands in contrast to the still widely used back-shifted Fermi-gas. The latter model fails to properly describe the data. Although the limited excitation energy region accessible does not allow a conclusive decision between the two models for ^{240}Pu, on a macroscopic level the nucleus is similar enough to the previously analyzed actinides that a constant temperature behavior for the level density is strongly suggested.

The spin distribution has been a major source of uncertainty in the extraction of the γ-ray strength function. However, further research on the actually transfered spin in light-ion, e.g. (d, p), reactions would be of great benefit in order to reduce the systematic errors.

The resulting γ-ray strength function shows an excess strength on the tail of the Giant Electric Dipole Resonance (GEDR) between 1 - 4 MeV that is interpreted as the scissors resonance in the quasicontinuum. The scissors mode appears to be double humped

with an average centroid $\omega_{\mathrm{SR}} = 2.15(6)\,\mathrm{MeV}$ and the derived summed $B(M1)$ strength is $B(M1) = 11.0(16)\,\mu_{\mathrm{N}}^2$. This is similar to previous analyses of actinides using the Oslo method for $^{231-233}$Th, $^{232-233}$Pa, $^{237-239}$U [13–15], ^{238}Np [16] and ^{243}Pu [17]. Experiments using (γ, γ') and (e, e') reactions typically yield about 2-3 times lower strength and two hypotheses for the differences have been discussed.

Finally, the obtained level density and γ-ray strength function have been used together with the optical model potential of Soukhovitskii et al. [79] to calculated the neutron capture cross-section of ^{239}Pu using the TALYS [25] nuclear reactions code. We expect a considerable impact of the calculation for the study of fast neutron reactors and in the nucleosynthesis of heavy elements. It is therefore of particular importance to correct the demonstrated inconsistencies in the computational implementation of the optical model potential. Once these are resolved, it is expected that our calculations lead to significantly more reliable (n, γ) cross-sections for fast neutrons.

To our knowledge, neither the scissors resonance nor the upbend have up to now been included in astrophysical models of e.g. the nucleosynthesis of heavy elements. Two recently initiated projects have started to address in depth the effect of these additional resonances on (n, γ) cross-sections and the impact on applications in reactor and astrophysics. The analysis is based on the results found in this work, previous findings using the Oslo Method, and systematics that can be derived from these.

In order to strengthen our knowledge on properties of heavy nuclei we will investigate further nuclear reaction on actinides targets. In 2016, experiments with ^{240}Pu, ^{244}Pu and ^{237}Np targets are planed. Recently, a new technique has been developed that uses γ-ray spectra following β-decay [89]. This further increases the already wide range of accessible nuclei. At the OCL the NaI detectors will be replaced by large volume $LaBr_3$:Ce detectors, which are superior in timing, efficiency and energy resolution. This provides the possibility for a more detailed study of the γ-ray strength function including the search for a potential fine structure in the scissors resonance.

Appendix A.

A Appendix

A.1. Experimental set-up and data extraction

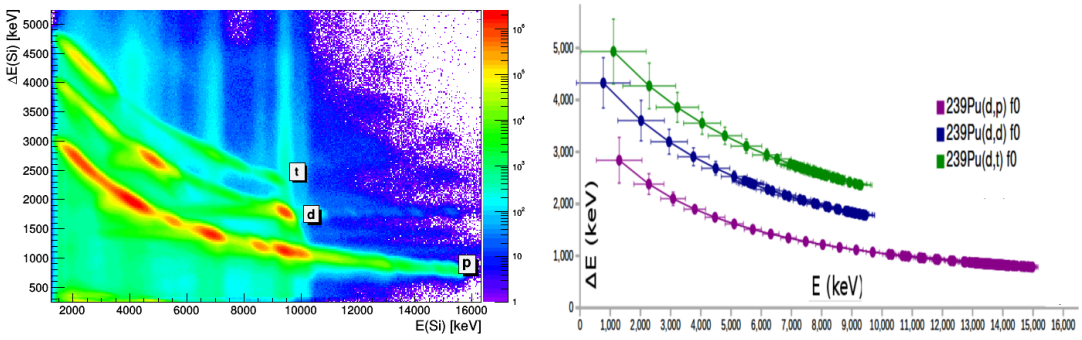

(a) (b)

Figure A.1.: (a) Energy deposited in SiRi's front and back detectors, E and ΔE respectively. (b) Corresponding spectrum calculated with "SiRi Kinematics Calculator" for $\Theta = 140°$.

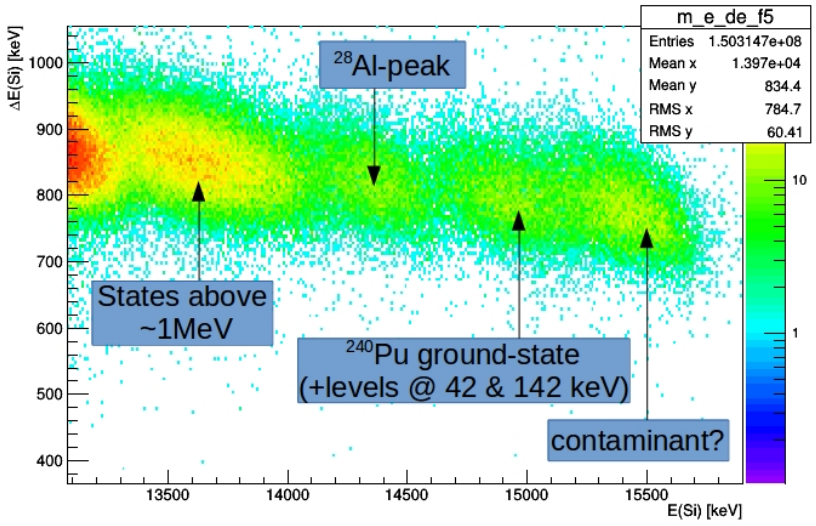

Figure A.2.: Energy deposited in SiRi's front and back detectors, E and ΔE respectively, at $\theta = 140°$. The plot is zoomed in on the region close to the (d, p) ground state. A brief explanation of the peaks is given as insets in the Figure. Because of the detector resolution, the levels at 42 and 142 keV fall together with the ground-state. More information can be found in Chapter 2.

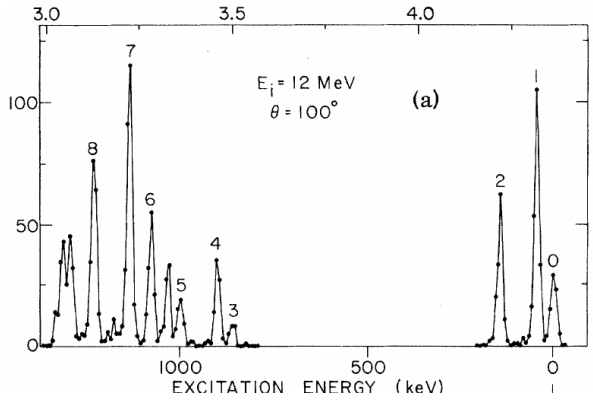

Figure A.3.: Magnetic spectrum for the reaction ^{239}Pu(d,p)^{240}Pu with 12 MeV deuterons at a scattering angle of 100°. The y-axis gives the reaction intensity in arbitrary units. Observe the approximately 600 keV wide region that contains little to no counts. Reproduced from [42].

Table A.1.: New intensities and FWHM obtained for the NaI response function **R**. Source: M. Guttormsen (UiO), priv. comm., 03.02.2015.

E_γ [keV]	FWHM [a] [keV]	ϵ_{tot} [b]	p_f	p_c	p_s	p_d	p_a
252	33.7	0.7660	0.8140	0.1860	0.0000	0.0000	0.0000
572	62.2	0.8680	0.7061	0.2939	0.0000	0.0000	0.0000
892	76.1	0.9450	0.6045	0.3947	0.0009	0.0000	0.0000
1212	85.9	0.9830	0.4962	0.4966	0.0072	0.0000	0.0000
1532	100.2	1.0010	0.4203	0.5669	0.0095	0.0000	0.0033
1852	113.3	1.0110	0.3655	0.6158	0.0119	0.0000	0.0069
2172	127.0	1.0180	0.3349	0.6381	0.0154	0.0000	0.0115
2492	138.9	1.0250	0.3019	0.6632	0.0189	0.0000	0.0160
2812	149.1	1.0310	0.2672	0.6902	0.0222	0.0000	0.0204
3132	161.5	1.0360	0.2473	0.6918	0.0330	0.0070	0.0208
3452	172.3	1.0400	0.2288	0.6971	0.0372	0.0076	0.0294
3772	182.0	1.0430	0.2097	0.7031	0.0413	0.0081	0.0378
4092	190.6	1.0460	0.1911	0.7082	0.0455	0.0088	0.0465
4412	198.2	1.0490	0.1705	0.7163	0.0492	0.0093	0.0547
4732	205.7	1.0520	0.1609	0.7242	0.0519	0.0092	0.0537
5052	212.7	1.0550	0.1540	0.7342	0.0539	0.0089	0.0490
5372	218.9	1.0580	0.1478	0.7429	0.0561	0.0086	0.0446
5692	224.1	1.0600	0.1409	0.7528	0.0580	0.0082	0.0400
6012	228.5	1.0630	0.1341	0.7627	0.0599	0.0079	0.0354
6332	236.4	1.0650	0.1292	0.7685	0.0590	0.0080	0.0353
6652	246.6	1.0670	0.1256	0.7716	0.0565	0.0083	0.0380
6972	256.5	1.0700	0.1223	0.7742	0.0541	0.0086	0.0407
7292	266.3	1.0710	0.1183	0.7780	0.0514	0.0089	0.0433
7612	276.0	1.0720	0.1144	0.7818	0.0488	0.0092	0.0459
7932	285.4	1.0730	0.1102	0.7859	0.0460	0.0095	0.0484
8252	294.7	1.0740	0.1063	0.7896	0.0433	0.0098	0.0510
8572	303.8	1.0750	0.1024	0.7932	0.0407	0.0101	0.0536
8892	312.8	1.0760	0.0983	0.7973	0.0379	0.0104	0.0561
9212	321.5	1.0770	0.0942	0.8013	0.0352	0.0107	0.0586
9532	330.1	1.0780	0.0903	0.8051	0.0325	0.0110	0.0611
9852	338.6	1.0800	0.0859	0.8097	0.0297	0.0112	0.0634
10172	346.4	1.0800	0.0838	0.8122	0.0300	0.0112	0.0628
10492	354.0	1.0810	0.0822	0.8140	0.0308	0.0113	0.0618
10812	361.4	1.0820	0.0802	0.8165	0.0316	0.0112	0.0605
11132	368.6	1.0820	0.0783	0.8189	0.0323	0.0112	0.0592
11452	375.6	1.0830	0.0764	0.8214	0.0331	0.0112	0.0580
11772	382.4	1.0840	0.0743	0.8241	0.0338	0.0112	0.0566
12092	389.0	1.0840	0.0726	0.8262	0.0346	0.0112	0.0555
12412	395.4	1.0850	0.0706	0.8288	0.0353	0.0112	0.0542
12732	401.6	1.0850	0.0687	0.8312	0.0360	0.0111	0.0529
13052	407.6	1.0860	0.0667	0.8339	0.0367	0.0111	0.0516
13372	413.4	1.0870	0.0648	0.8361	0.0375	0.0111	0.0504
13692	419.0	1.0870	0.0629	0.8386	0.0382	0.0111	0.0492

[a] Normalized to 79.9 keV (6 %) at 1.33 MeV.

[b] Arbitrary normalization to 1 at 1.33 MeV

A.2. Resonance parametrization: SLO and EGLO

Over the time a manifold of different formulas were developed to fit resonances in the γ-ray strength function. The basic starting point is usually the standard Lorentzian f_{SLO} [52], which is derived from the response of a dampened harmonic oscillator [90]

$$f_{\mathrm{SLO}}(E_\gamma) = \frac{1}{3\pi\hbar^2c^2}\sigma_{\mathrm{r}}\Gamma_{\mathrm{r}}\frac{E_\gamma\,\Gamma_{\mathrm{r}}}{(E_\gamma^2 - E_r^2)^2 + E_\gamma^2\Gamma_{\mathrm{r}}}, \tag{A.1}$$

where σ_r, Γ_r and E_r are the cross-section, full width at half maximum and energy of the resonance.

In order to improve the agreement with certain experimental observations, many studies have included additional terms. In this work we use the Enhanced Generalized Lorentzian f_{EGLO} [91, 92] for the Giant Dipole Resonances, which i.a. takes into account the temperature of final states T_f

$$f_{\mathrm{EGLO}} = \frac{1}{3\pi\hbar^2c^2}\sigma_{\mathrm{r}}\Gamma_{\mathrm{r}}\left[\frac{E_\gamma\,\Gamma(E_\gamma,T_f)}{(E_\gamma^2 - E_r^2)^2 + E_\gamma^2\Gamma^2(E_\gamma,T_f)} + 0.7\frac{\Gamma(E_\gamma=0,T_f)}{E_r^3}\right], \tag{A.2}$$

where

$$\Gamma(E_\gamma,T_f) = \frac{\Gamma_r}{E_r^3}(E_\gamma^2 + 4\pi^2T_f^2). \tag{A.3}$$

For a more detailed discussion of the different models in relation to the γ-ray strength function, see Ref. [37].

Bibliography

[1] E. Rutherford. The scattering of α and β particles by matter and the structure of the atom. *Philosophical Magazine*, 21(6):669–688, 1911. ISSN 1478-6443. doi: 10.1080/14786435.2011.617037.

[2] J. Chadwick. The Existence of a Neutron. *Proceedings of the Royal Society A: Mathematical, Physical and Engineering Sciences*, 136(830):692–708, June 1932. ISSN 1471-2946. doi: 10.1098/rspa.1932.0112.

[3] E. Fermi, E. Amaldi, O. D'Agostino, F. Rasetti, and E. Segre. Artificial Radioactivity Produced by Neutron Bombardment. *Proceedings of the Royal Society A: Mathematical, Physical and Engineering Sciences*, 146(857):483–500, September 1934. ISSN 1471-2946. doi: 10.1098/rspa.1934.0168.

[4] L. Meitner and O. R. Frisch. Disintegration of Uranium by Neutrons: a New Type of Nuclear Reaction. *Nature*, 143(3615):239–240, February 1939. ISSN 0028-0836. doi: 10.1038/143239a0.

[5] Y. Alhassid, L. Fang, and H. Nakada. Heavy Deformed Nuclei in the Shell Model Monte Carlo Method. *Physical Review Letters*, 101(8), August 2008. ISSN 1079-7114. doi: 10.1103/physrevlett.101.082501.

[6] S. Goriely, S. Hilaire, and A. J. Koning. Improved microscopic nuclear level densities within the Hartree-Fock-Bogoliubov plus combinatorial method. *Physical Review C*, 78 (6), December 2008. ISSN 1089-490X. doi: 10.1103/physrevc.78.064307.

[7] J. M. Blatt and V. F. Weisskopf. *Theoretical Nuclear Physics*. Wiley [u.a.], New York, 1952.

[8] H. K. Vonach and J. R. Huizenga. Co59 (p, α) Fe56 and Fe56 (p, p') Reactions. *Physical Review*, 149(3):844–853, September 1966. ISSN 0031-899X. doi: 10.1103/physrev.149.844.

[9] A.M. Hoogenboom. A new method in gamma-ray spectroscopy: A two crystal scintillation spectrometer with improved resolution. *Nuclear Instruments*, 3(2):57–68, August 1958. ISSN 0369-643X. doi: 10.1016/0369-643x(58)90092-6.

[10] Y. Kalmykov, C. Özen, K. Langanke, G. Martínez-Pinedo, P. von Neumann-Cosel, and A. Richter. Spin- and Parity-Resolved Level Densities from the Fine Structure of Giant Resonances. *Physical Review Letters*, 99(20), November 2007. ISSN 1079-7114. doi: 10.1103/physrevlett.99.202502.

[11] A Schiller, L Bergholt, M Guttormsen, E Melby, J Rekstad, and S Siem. Extraction of level density and γ strength function from primary γ spectra. *Nucl. Instrum. Methods Phys. Res. A*, 447(3):498–511, June 2000. ISSN 0168-9002. doi: 10.1016/s0168-9002(99)01187-0.

[12] A. C. Larsen, M. Guttormsen, M. Krtička, E. Běták, A. Bürger, A. Görgen, H. T. Nyhus, J. Rekstad, A. Schiller, S. Siem, and et al. Analysis of possible systematic errors in the Oslo method. *Phys. Rev. C*, 83(3):034315, March 2011. ISSN 1089-490X. doi: 10.1103/physrevc.83.034315.

[13] M. Guttormsen, B. Jurado, J. N. Wilson, M. Aiche, L. A. Bernstein, Q. Ducasse, F. Giacoppo, A. Görgen, F. Gunsing, T. W. Hagen, and et al. Constant-temperature level densities in the quasicontinuum of Th and U isotopes. *Phys. Rev. C*, 88(2):024307, August 2013. ISSN 1089-490X. doi: 10.1103/physrevc.88.024307.

[14] M. Guttormsen, L. A. Bernstein, A. Görgen, B. Jurado, S. Siem, M. Aiche, Q. Ducasse, F. Giacoppo, F. Gunsing, T. W. Hagen, and et al. Scissors resonance in the quasicontinuum of Th, Pa, and U isotopes. *Phys. Rev. C*, 89(1):014302, January 2014. ISSN 1089-490X. doi: 10.1103/physrevc.89.014302.

[15] M. Guttormsen, L. A. Bernstein, A. Bürger, A. Görgen, F. Gunsing, T. W. Hagen, A. C. Larsen, T. Renstrøm, S. Siem, M. Wiedeking, and et al. Observation of Large Scissors Resonance Strength in Actinides. *Physical Review Letters*, 109(16), October 2012. ISSN 1079-7114. doi: 10.1103/physrevlett.109.162503.

[16] T. G. Tornyi, M. Guttormsen, T. K. Eriksen, A. Görgen, F. Giacoppo, T. W. Hagen, A. Krasznahorkay, A. C. Larsen, T. Renstrøm, S. J. Rose, and et al. Level density and γ-ray strength function in the odd-odd ^{238}Np nucleus. *Phys. Rev. C*, 89(4):044323, April 2014. ISSN 1089-490X. doi: 10.1103/physrevc.89.044323.

[17] T. A. Laplace, F. Zeiser, M. Guttormsen, A. C. Larsen, D. L. Bleuel, L. A. Bernstein, B. L. Goldblum, S. Siem, F. L. Bello Garotte, J. A. Brown, and et al. Statistica properties of ^{243}Pu, and ^{242}Pu(n,γ) cross section calculation. *Physical Review C*, 93(1), January 2016. ISSN 2469-9993. doi: 10.1103/physrevc.93.014323.

[18] H. A. Bethe. An Attempt to Calculate the Number of Energy Levels of a Heavy Nucleus. *Physical Review*, 50(4):332–341, August 1936. ISSN 0031-899X. doi: 10.1103/physrev.50.332.

[19] R. Capote, M. Herman, P. Obložinský, P.G. Young, S. Goriely, T. Belgya, A.V. Ignatyuk, A.J. Koning, S. Hilaire, V.A. Plujko, and et al. RIPL – Reference Input Parameter Library for Calculation of Nuclear Reactions and Nuclear Data Evaluations. *Nuclear Data Sheets*, 110(12):3107–3214, December 2009. ISSN 0090-3752. doi: 10.1016/j.nds.2009.10.004. Data extraced from RIPL-3 online database https://www-nds.iaea.org/RIPL-3/, accessed 10.05.2015.

[20] F. W. K. Firk. Low-Energy Photonuclear Reactions. *Annu. Rev. Nucl. Sci.*, 20(1):39–78, December 1970. ISSN 0066-4243. doi: 10.1146/annurev.ns.20.120170.000351.

[21] R. D. Heil, H. H. Pitz, U. E. P. Berg, U. Kneissl, K. D. Hummel, G. Kilgus, D. Bohle, A. Richter, C. Wesselborg, and P. Von Brentano. Observation of orbital magnetic dipole strength in the actinide nuclei 232Th and 238U. *Nuclear Physics A*, 476(1):39–47, January 1988. ISSN 0375-9474. doi: 10.1016/0375-9474(88)90371-5.

[22] J. Margraf, A. Degener, H. Friedrichs, R. D. Heil, A. Jung, U. Kneissl, S. Lindenstruth, H. H. Pitz, H. Schacht, U. Seemann, and et al. Photoexcitation of low-lying dipole transitions in U 236. *Physical Review C*, 42(2):771–774, August 1990. ISSN 1089-490X. doi: 10.1103/physrevc.42.771.

[23] O. Yevetska, J. Enders, M. Fritzsche, P. von Neumann-Cosel, S. Oberstedt, A. Richter, C. Romig, D. Savran, and K. Sonnabend. Dipole strength in the U 235 (γ, γ') reaction up to 2 . 8 MeV. *Physical Review C*, 81(4), April 2010. ISSN 1089-490X. doi: 10.1103/physrevc.81.044309.

[24] K. Heyde, P. von Neumann-Cosel, and A. Richter. Magnetic dipole excitations in nuclei: Elementary modes of nucleonic motion. *Rev. Mod. Phys.*, 82(3):2365–2419, September 2010. ISSN 1539-0756. doi: 10.1103/revmodphys.82.2365.

[25] A. J. Koning, S. Hilaire, and M. C. Duijvestijn. TALYS-1.0. In O. Bersillon, F. Gunsing, E. Bauge, R. Jacqmin, , and S. Leray, editors, *Proceedings of the International Conference on Nuclear Data for Science and Technology 2007*, page 211. EDP Sciences, April 2008.

[26] M.B. Chadwick, M. Herman, P. Obložinský, M.E. Dunn, Y. Danon, A.C. Kahler, D.L. Smith, B. Pritychenko, G. Arbanas, R. Arcilla, and et al. ENDF/B-VII.1 Nuclear Data for Science and Technology: Cross Sections, Covariances, Fission Product Yields and Decay Data. *Nuclear Data Sheets*, 112(12):2887–2996, December 2011. ISSN 0090-3752. doi: 10.1016/j.nds.2011.11.002.

[27] K. Shibata, O. Iwamoto, T. Nakagawa, N. Iwamoto, A. Ichihara, S. Kunieda, S. Chiba, K. Furutaka, N. Otuka, T. Ohasawa, and et al. JENDL-4.0: A New Library for Nuclear Science and Engineering. *Journal of Nuclear Science and Technology*, 48(1):1–30, January 2011. ISSN 1881-1248. doi: 10.1080/18811248.2011.9711675.

[28] H. Harada et al. Uncertainty and target accuracy assessment for innovative systems using recent covariance data evaluations. Technical Report Volume 31, NEA/NSC/WPEC/DOC(2014)446, OECD/NEA WPEC, 2014. URL `https://www.oecd-nea.org/science/wpec/volume31/volume31.pdf`.

[29] M. Salvatores et al. Uncertainty and target accuracy assessment for innovative systems using recent covariance data evaluations. Technical Report Volume 26, OECD/NEA WPEC, 2008. URL `https://www.oecd-nea.org/science/wpec/volume26/volume26.pdf`.

[30] M. Arnould, S. Goriely, and K. Takahashi. The r-process of stellar nucleosynthesis: Astrophysics and nuclear physics achievements and mysteries. *Physics Reports*, 450(4-6): 97–213, September 2007. ISSN 0370-1573. doi: 10.1016/j.physrep.2007.06.002.

[31] Oslo Cyclotron Laboratory Website. accessed 19.11.2014. URL `http://www.mn.uio.no/fysikk/english/research/about/infrastructure/OCL/`.

[32] R.A. Henderson, J.M. Gostic, J.T. Burke, S.E. Fisher, and C.Y. Wu. Electrodeposition of U and Pu on thin C and Ti substrates. *Nuclear Instruments and Methods in Physics Research Section A: Accelerators, Spectrometers, Detectors and Associated Equipment*, 655(1):66–71, November 2011. ISSN 0168-9002. doi: 10.1016/j.nima.2011.06.023.

[33] M. Guttormsen, A. Bürger, T.E. Hansen, and N. Lietaer. The SiRi particle-telescope system. *Nucl. Instrum. Methods Phys. Res. A*, 648(1):168–173, August 2011. ISSN 0168-9002. doi: 10.1016/j.nima.2011.05.055.

[34] M. Guttormsen, A. Atac, G. Løvhøiden, S. Messelt, T. Ramsøy, J. Rekstad, T. F. Thorsteinsen, T. S. Tveter, and Z. Zelazny. Statistical Gamma-Decay at Low Angular Momentum. *Phys. Scr.*, T32:54–60, January 1990. ISSN 1402-4896. doi: 10.1088/0031-8949/1990/t32/010.

[35] T. G. Tornyi, A. Görgen, M. Guttormsen, A. C. Larsen, S. Siem, A. Krasznahorkay, and L. Csige. A new fission-fragment detector to complement the CACTUS-SiRi setup at the Oslo Cyclotron Laboratory. *Nucl. Instrum. Methods Phys. Res. A*, 738:6–12, February 2014. ISSN 0168-9002. doi: 10.1016/j.nima.2013.12.005.

[36] Q. Ducasse, B. Jurado, M. Aïche, P. Marini, L. Mathieu, A. Görgen, M. Guttormsen, A. C. Larsen, T. Tornyi, J. N. Wilson, G. Barreau, G. Boutoux, S. Czajkowski, F. Giacoppo, F. Gunsing, T.W. Hagen, M. Lebois, J. Lei, V. Méot, B. Morillon, A. Moro, T. Renstrøm, O. Roig, S. J. Rose, O. Sérot, S. Siem, I. Tsekhanovich, G. M. Tveten, and M. Wiedeking. Study of the $^{2}38\mathrm{U}(\mathrm{d},\mathrm{p})$ surrogate reaction via the simultaneous measurement of gamma-decay and fission probabilities. 2015. URL `http://arxiv.org/abs/1512.06334`. Published on arXiv.

[37] Ann-Cecilie Larsen. *Statistical properties in the quasi-continuum of atomic nuclei.* PhD thesis, University of Oslo, 2008.

[38] H. Bethe. Bremsformel für Elektronen relativistischer Geschwindigkeit. *Zeitschrift für Physik*, 76(5-6):293–299, May 1932. ISSN 1434-601X. doi: 10.1007/bf01342532.

[39] J. F. Ziegler. Stopping of energetic light ions in elemental matter. *Journal of Applied Physics*, 85(3):1249–1272, 1999. doi: 10.1063/1.369844.

[40] A. Bürger. SiRi Kinematics Calculator. URL `https://unarydigits.com/jkinz/calculate#`. Accessed on 19.11.2014.

[41] T. Grotdal, L. Løset, K. Nybø, and T.F. Thorsteinsen. Energy levels in 237Pu and 239Pu. *Nuclear Physics A*, 211(3):541–558, September 1973. ISSN 0375-9474. doi: 10.1016/0375-9474(73)90442-9.

[42] A. Friedman and K. Katori. Population of 0^+ Excited States in ^{238}Pu and ^{240}Pu by Single-Neutron Transfer Reactions. *Physical Review Letters*, 30(3):102–105, January 1973. ISSN 0031-9007. doi: 10.1103/physrevlett.30.102.

[43] D. R. Tilley, H. R. Weller, and C. M. Cheves. Energy levels of light nuclei A = 16–17. *Nuclear Physics A*, 564(1):1–183, November 1993. doi: 10.1016/0375-9474(93)90073-7. Data extracted from the ENSDF database, version Feburary 1999.

[44] D. R. Tilley, J. H. Kelley, J. L. Godwin, D. J. Millener, J. E. Purcell, C. G. Sheu, and H. R. Weller. Energy levels of light nuclei. *Nuclear Physics A*, 745(3-4):155–362, December 2004. doi: 10.1016/j.nuclphysa.2004.09.059. Data extracted from the ENSDF database, version May 2007.

[45] Wikimedia Commons. Constant fraction discriminator, 2006. URL `https://upload.wikimedia.org/wikipedia/commons/8/8f/Constant_fraction_1.svg`. Accessed on 17. December 2014.

[46] Balraj Singh and E. Browne. Nuclear Data Sheets for A = 240. *Nuclear Data Sheets*, 109(10):2439–2499, October 2008. ISSN 0090-3752. doi: 10.1016/j.nds.2008.09.002. Data extracted from the ENSDF database, version November 2010.

[47] G. N. Smirenkin. Preparation of Evaluated Data for a Fission Barrier Parameter Library for Isotopes with Z = 82 - 98, with Consideration of the Level Density Models Used. Technical Report IAEA-Report INDC(CCP)-359, 1993. URL `https://www-nds.iaea.org/RIPL-3/`. Translated from an unpublished manuscript. Data extracted from the RIPL 3 database, version January 2009.

[48] K. Nishio, H. Ikezoe, Y. Nagame, S. Mitsuoka, I. Nishinaka, L. Duan, K. Satou, M. Asai, H. Haba, K. Tsukada, N. Shinohara, S. Ichikawa, and T. Ohsawa. Fragment Mass Distribution of the 239Pu(d,pf) Reaction at the Super-deformed Beta-vibrational Resonance. In Takaaki OHSAWA and Tokio FUKAHORI, editors, *Proceedings of the 2002 Symposium on Nuclear Data. November 21-22, 2002, JAERI, Tokai, Japan*, 2003.

[49] B. B. Back, Ole Hansen, H. C. Britt, and J. D. Garrett. Fission of doubly even actinide nuclei induced by direct reactions. *Physical Review C*, 9(5):1924–1947, May 1974. ISSN 0556-2813. doi: 10.1103/physrevc.9.1924.

[50] M Guttormsen, T.S Tveter, L Bergholt, F Ingebretsen, and J Rekstad. The unfolding of continuum γ-ray spectra. *Nucl. Instrum. Methods Phys. Res. A*, 374(3):371–376, June 1996. ISSN 0168-9002. doi: 10.1016/0168-9002(96)00197-0.

[51] M. Guttormsen, T. Ramsøy, and J. Rekstad. The first generation of γ-rays from hot nuclei. *Nucl. Instrum. Methods Phys. Res. A*, 255(3):518–523, April 1987. ISSN 0168-9002. doi: 10.1016/0168-9002(87)91221-6.

[52] D. M. Brink. *Ph.D. thesis*. PhD thesis, Oxford University, 1955. unpublished.

[53] P. Axel. Electric Dipole Ground-State Transition Width Strength Function and 7-Mev Photon Interactions. *Phys. Rev.*, 126(2):671–683, April 1962. ISSN 1536-6065. doi: 10.1103/physrev.126.671.

[54] L. Henden, L. Bergholt, M. Guttormsen, J. Rekstad, and T.S. Tveter. On the relation between the statistical γ-decay and the level density in 162Dy. *Nuclear Physics A*, 589 (2):249–266, July 1995. ISSN 0375-9474. doi: 10.1016/0375-9474(95)00133-l.

[55] T. Tveter, L. Bergholt, M. Guttormsen, E. Melby, and J. Rekstad. Observation of Fine Structure in Nuclear Level Densities and γ-Ray Strength Functions. *Physical Review Letters*, 77(12):2404–2407, September 1996. ISSN 1079-7114. doi: 10.1103/physrevlett.77.2404.

[56] Data extracted from the ENDSF database using NNDC's Chart of Nuclides, http://www.nndc.bnl.gov/chart/. accessed 10.05.2015.

[57] A. Gilbert and A. G. W. Cameron. A Composite Nuclear-level Density Formula With Shell Corrections. *Canadian Journal of Physics*, 43(8):1446–1496, August 1965. ISSN 1208-6045. doi: 10.1139/p65-139.

[58] T. von Egidy and D. Bucurescu. Systematics of nuclear level density parameters. *Phys. Rev. C*, 72(4):044311, October 2005. doi: 10.1103/physrevc.72.044311. Phys. Rev. C 73, 049901(E) (2006), Doi:.

[59] J. Kopecky and M. Uhl. Test of gamma-ray strength functions in nuclear reaction model calculations. *Physical Review C*, 41(5):1941–1955, May 1990. ISSN 1089-490X. doi: 10.1103/physrevc.41.1941.

[60] M. A. Lone. Photon Strength Functions. *Neutron Induced Reactions. Proceedings of the 4th International Symposium Smolenice, Czechoslovakia, June 1985*, page 238–252, 1986. doi: 10.1007/978-94-009-4636-1_26.

[61] G.M. Gurevich, L.E. Lazareva, V.M. Mazur, G.V. Solodukhov, and B.A. Tulupov. Giant resonance in the total photoabsorption cross section of Z $\approx$ 90 nuclei. *Nuclear Physics A*, 273(2):326–340, November 1976. ISSN 0375-9474. doi: 10.1016/0375-9474(76)90594-7.

[62] J. Caldwell, E. Dowdy, B. Berman, R. Alvarez, and P. Meyer. Giant resonance for the actinide nuclei: Photoneutron and photofission cross sections for ^{235}U, ^{236}U, ^{238}U, and ^{232}Th. *Phys. Rev. C*, 21(4):1215–1231, April 1980. ISSN 0556-2813. doi: 10.1103/physrevc.21.1215.

[63] M. A. P. V. De Moraes and M. F. Cesar. Photonuclear cross sections of Pu-239 Using neutron capture gamma rays, near threshold. *Phys. Scr.*, 47(4):519–523, April 1993. ISSN 1402-4896. doi: 10.1088/0031-8949/47/4/008.

[64] E. Lipparini and S. Stringari. Sum rules and giant resonances in nuclei. *Physics Reports*, 175(3-4):103–261, April 1989. ISSN 0370-1573. doi: 10.1016/0370-1573(89)90029-x.

[65] J. Enders, P. von Neumann-Cosel, C. Rangacharyulu, and A. Richter. Parameter-free description of orbital magnetic dipole strength. *Physical Review C*, 71(1), January 2005. ISSN 1089-490X. doi: 10.1103/physrevc.71.014306.

[66] F. Bečvář. Simulation of γ cascades in complex nuclei with emphasis on assessment of uncertainties of cascade-related quantities. *Nuclear Instruments and Methods in Physics Research Section A: Accelerators, Spectrometers, Detectors and Associated Equipment*, 417(2-3):434–449, November 1998. ISSN 0168-9002. doi: 10.1016/s0168-9002(98)00787-6.

[67] E. Běták. Cluster-γ competition in the Iwamoto-Harada-Bisplinghoff model. *EPJ Web of Conferences*, 2:11002, 2010. ISSN 2100-014X. doi: 10.1051/epjconf/20100211002.

[68] A.J. Koning and J.M. Akkermans. Pre-equilibrium nuclear reactions: An introduction to classical and quantum-mechanical mode. ICTP Workshop, 1998. URL `ftp://ftp.nrg.eu/pub/www/talys/bib_koning/1998_Koning_preeq_ICTP.pdf`.

[69] M. Guttormsen, R. Chankova, U. Agvaanluvsan, E. Algin, L. A. Bernstein, F. Ingebretsen, T. Lönnroth, S. Messelt, G. E. Mitchell, J. Rekstad, and et al. Radiative strength functions in Mo 93 – 98. *Physical Review C*, 71(4), April 2005. ISSN 1089-490X. doi: 10.1103/physrevc.71.044307.

[70] M. Guttormsen, A. Bagheri, R. Chankova, J. Rekstad, S. Siem, A. Schiller, and A. Voinov. Thermal properties and radiative strengths in Dy 160 , 161 , 162. *Physical Review C*, 68 (6), December 2003. ISSN 1089-490X. doi: 10.1103/physrevc.68.064306.

[71] U. Agvaanluvsan, A. Schiller, J. A. Becker, L. A. Bernstein, P. E. Garrett, M. Guttormsen, G. E. Mitchell, J. Rekstad, S. Siem, A. Voinov, and et al. Level densities and γ-ray strength functions in Yb 170 , 171 , 172. *Physical Review C*, 70(5), November 2004. ISSN 1089-490X. doi: 10.1103/physrevc.70.054611.

[72] H. T. Nyhus, S. Siem, M. Guttormsen, A. C. Larsen, A. Bürger, N. U. H. Syed, G. M. Tveten, and A. Voinov. Radiative strength functions in Dy 163 , 164. *Physical Review C*, 81(2), February 2010. ISSN 1089-490X. doi: 10.1103/physrevc.81.024325.

[73] A. Voinov, E. Algin, U. Agvaanluvsan, T. Belgya, R. Chankova, M. Guttormsen, G. E. Mitchell, J. Rekstad, A. Schiller, and S. Siem. Large Enhancement of Radiative Strength for Soft Transitions in the Quasicontinuum. *Physical Review Letters*, 93(14), September 2004. ISSN 1079-7114. doi: 10.1103/physrevlett.93.142504.

[74] A. C. Larsen, M. Guttormsen, R. Chankova, F. Ingebretsen, T. Lönnroth, S. Messelt, J. Rekstad, A. Schiller, S. Siem, N. U. H. Syed, and et al. Nuclear level densities and γ-ray strength functions in Sc 44 , 45. *Physical Review C*, 76(4), October 2007. ISSN 1089-490X. doi: 10.1103/physrevc.76.044303.

[75] M. Guttormsen, A. C. Larsen, A. Görgen, T. Renstrøm, S. Siem, T. G. Tornyi, and G. M. Tveten. Validity of the Generalized Brink-Axel Hypothesis in Np 238. *Physical Review Letters*, 116(1), January 2016. ISSN 1079-7114. doi: 10.1103/physrevlett.116.012502.

[76] T. von Egidy and D. Bucurescu. Experimental energy-dependent nuclear spin distributions. *Phys. Rev. C*, 80(5):054310, November 2009. ISSN 1089-490X. doi: 10.1103/physrevc.80.054310.

[77] N. U. H. Syed, A. C. Larsen, A. Bürger, M. Guttormsen, S. Harissopulos, M. Kmiecik, T. Konstantinopoulos, M. Krtička, A. Lagoyannis, T. Lönnroth, and et al. Extraction of thermal and electromagnetic properties in Ti 45. *Physical Review C*, 80(4), October 2009. ISSN 1089-490X. doi: 10.1103/physrevc.80.044309.

[78] E. Algin, U. Agvaanluvsan, M. Guttormsen, A. C. Larsen, G. E. Mitchell, J. Rekstad, A. Schiller, S. Siem, and A. Voinov. Thermodynamic properties of Fe 56 , 57. *Physical Review C*, 78(5), November 2008. ISSN 1089-490X. doi: 10.1103/physrevc.78.054321.

[79] Efrem Sh Soukhovitskii, Satoshi Chiba, Jeong-Yeon Lee, Osamu Iwamoto, and Tokio Fukahori. Global coupled-channel optical potential for nucleon–actinide interaction from 1 keV to 200 MeV. *J. Phys. G: Nucl. Part. Phys.*, 30(7):905–920, May 2004. ISSN 1361-6471. doi: 10.1088/0954-3899/30/7/007.

[80] A.J. Koning and J.P. Delaroche. Local and global nucleon optical models from 1 keV to 200 MeV. *Nuclear Physics A*, 713(3-4):231–310, January 2003. ISSN 0375-9474. doi: 10.1016/s0375-9474(02)01321-0.

[81] S.F Mughabghab and C.L Dunford. A dipole–quadrupole interaction term in E1 photon transitions. *Physics Letters B*, 487(1-2):155–164, August 2000. ISSN 0370-2693. doi: 10.1016/s0370-2693(00)00792-9.

[82] J. C. Hopkins and B. C. Diven. Neutron Capture to Fission Ratios in ^{233}U, ^{235}U, ^{239}Pu. *Nuclear Science and Engineering*, 12:169, 1962. Data retrieved from the EXFOR database, file EXFOR 12331:1 dated Oct 05, 1984.

[83] V. N. Kononov, E. D. Poletayev, and B. D. Yurlov. The Measurement of Alpha, Neutron Fission and Capture Cross Sections for Uranium-235 and Plutonium-239 for Neutron Energies from 10 to 80 keV. *Atomnaya Energiya*, 38(2):82, 1975. Data retrieved from the EXFOR database, file EXFOR 40300:1 and 40412:1 dated Mar 25, 2014.

[84] M. G. Schomberg, M. G. Sowerby, D. A. Boyce, K. J. Murray, and D. L. Sutton. Ratio Of The Capture And Fission Cross-sections Of Pu-239 In The Energy Range 100 Ev To 30 Kev. In *Nuclear Data for Reactors Conference, Helsinki 1970*, volume 1, page 315, 1970. Data retrieved from the EXFOR database, file EXFOR 20476:1 dated Jan 20, 1984.

[85] A. V. Voinov, B. M. Oginni, S. M. Grimes, C. R. Brune, M. Guttormsen, A. C. Larsen, T. N. Massey, A. Schiller, and S. Siem. Nuclear excitations at constant temperature. *Physical Review C*, 79(3), March 2009. ISSN 1089-490X. doi: 10.1103/physrevc.79.031301.

[86] T. Sumaryada and A. Volya. Thermodynamics of pairing in mesoscopic systems. *Physical Review C*, 76(2), August 2007. ISSN 1089-490X. doi: 10.1103/physrevc.76.024319.

[87] B.V. Kheswa, M. Wiedeking, F. Giacoppo, S. Goriely, M. Guttormsen, A.C. Larsen, F.L. Bello Garrote, T.K. Eriksen, A. Görgen, T.W. Hagen, and et al. Galactic production of 138La: Impact of 138,139La statistical properties. *Physics Letters B*, 744:268–272, May 2015. ISSN 0370-2693. doi: 10.1016/j.physletb.2015.03.065.

[88] S. L. Hammond, A. S. Adekola, C. T. Angell, H. J. Karwowski, E. Kwan, G. Rusev, A. P. Tonchev, W. Tornow, C. R. Howell, and J. H. Kelley. Dipole response of 238 U to polarized photons below the neutron separation energy. *Physical Review C*, 85(4), April 2012. ISSN 1089-490X. doi: 10.1103/physrevc.85.044302.

[89] A. Spyrou, S. N. Liddick, A. C. Larsen, M. Guttormsen, K. Cooper, A. C. Dombos, D. J. Morrissey, F. Naqvi, G. Perdikakis, S. J. Quinn, and et al. Novel technique for Constraining r -Process (n, γ) Reaction Rates. *Physical Review Letters*, 113(23), December 2014. ISSN 1079-7114. doi: 10.1103/physrevlett.113.232502.

[90] H. Steinwedel and J. H. D. Jensen. Hydrodynamik von Kerndipolschwingungen. *Z. Naturfoschg.*, 5a:413, 1950.

[91] J. Kopecky and R.E. Chrien. Observation of the $M1$ giant resonance by resonance averaging in ^{106}Pd. *Nuclear Physics A*, 468(2):285–300, 1987. ISSN 0375-9474. doi: 10.1016/0375-9474(87)90518-5.

[92] S.G. Kadmenskii, V.P. Markushev, and V.I. Furman. Radiative width of neutron resonances. Giant dipole resonances. *Sov. J. Nucl. Phys.*, 37:165, 1983.